Single Skin Kite Airfoil Optimization for AWES

R.J. Coenen

Technische Universiteit Delft

TU Delft

Single Skin Kite Airfoil Optimization for AWES

by

R.J. Coenen

to obtain the degree of Master of Science
at the Delft University of Technology,
to be defended publicly on Friday 21st December, 2018 at 14:00.

Student number:	1506862	
Project duration:	July 1, 2016–October 2017, October 2018 – December 21, 2018	
Thesis committee:	Dr.-Ing. Roland Schmehl,	TU Delft, supervisor
	ir. Nando Timmer,	TU Delft
	Dr. Arvind Gangoli Rao	TU Delft
	J. Breuer, MSc.,	Kitepower BV, external supervisor

This thesis is confidential and cannot be made public until 21-12-2020

TU Delft

Preface

The interest for the subject of this thesis started in 2014 when I performed my Bachelor thesis project (Design Synthesis Exercise) with Roland Schmehl. After the succesful project and winning the symposium where all the projects were presented, I started working for Roland as his student assistant. I worked on, among other things, organizing the Airborne Wind Energy Conference and helped with editing the second Airborne Wind Energy book. Doing my thesis at Kitepower therefore was a nice next step.

I would like to thank Roland Schmehl for the opportunities and guidance he gave me. Joep Breuer, thank you for the daily guidance, hard questions and the attempts to keep my project on schedule. Also thanks to Johannes Peschel, CEO of Kitepower, for the opportunity to do my thesis at Kitepower in the first place. A special thanks also goes out to Susan de Rouw for the all help en guidance.

Thank you, Birgit for all the love and support in the last six years already. And last but not least, I am very grateful towards my parents who made it possible to be here in the first place.

R.J. Coenen
Delft, December 2018

Summary

Airborne Wind Energy is a technology where wind energy is harvested with tethered flying devices. Kitepower uses flexible leading edge inflatable kites, but these have a scaling disadvantage in that they become heavier with size. A single skin kite has the potential of negating this disadvantage while at the same time being more aerodynamically efficient. An airfoil of this type is therefore investigated using Computational Fluid Dynamics and optimized using Surrogate Modelling techniques.

For the optimization process, an autonomous meshing strategy is developed using a combination of hyperbolic extrusion and Delauney triangulation. A closed surface is made with the airfoil and an arc and line section, which is extruded to the far field boundary and inward by 0.01c. The remaining cavity is filled in with triangles. The mesh regions are merged over the arc and line section, leaving the airfoil as a wall. A RANS analysis is performed with a k-ω SST turbulence model. No transition model is implemented, because it is assumed that in real-life the roughness of the kite cloth combined with seams and other perturbations force transition early on. In the mesh convergence study, it becomes clear that the airfoil requires a large amount of cells around its circumference. It is also concluded that, although it comes with a cell number penalty of approximately 10%, it is beneficial to have the domain boundary far away at 500c. The large domain ensures that perturbations to the flow by the airfoil dissipate before they interact with the boundary. This speeds up analysis significantly. Reliable wind tunnel data for this type of airfoil does not exist, so validation is performed on a NACA 2412 airfoil at $Re = 9 \cdot 10^6$. An adapted NACA 4-digit parametrization is used. The variables are maximum camber, location of maximum camber, maximum thickness, leading edge radius, location of maximum thickness and length of the bottom skin in chord wise direction. The analyses in the optimization are run at $Re = 14 \cdot 10^6$.

The SUMO toolbox is used for the surrogate modelling process. For the sequential design strategy, the LOLA-Voronoi algorithm is used, because it balances exploitation and exploration very well. This means it weighs regions of interest and sampling density. Standard Kriging is employed as the regression model. The objective function is an effective power factor derived from Loyd's power equation, in the form of $C_{\mathrm{L}}^3/C_{\mathrm{D,eff}}^2$. It also includes approximations for the kite shape and tether drag.

The final model provided no clear design directions. The airfoil scores were all very close to each other: the optimum airfoil performed only 5.38% better than the average of 9.417. It is concluded that the choice of parametrization was wrong. The variables have too much global control and do not produce unique airfoils, e.g. a thick airfoil with no camber can be approximated by a thinner airfoil with camber.

It is recommended to repeat the process with a different parametrization. It is advised to perform wind tunnel tests of single skin airfoils or similar kite airfoils for validation. Although very promising, it cannot be concluded if the surrogate modelling process is suitable for this application, due to the problems with the parametrization.

Contents

Nomenclature

Abbreviation	Description	Units
AoA	Angle of Attack	
AWE	Airborne Wind Energy	
AWES	Airborne Wind Energy System	
BL	Boundary Layer	
GA	Genetic Algorithm	
HAWT	Horizontal Axis Wind Turbine	
ISA	International Standard Atmosphere	
KCU	Kite Control Unit	
LE	Leading Edge	
RS	Response Surface	
RSM	Response Surface Method	
SM	Surrogate Modelling	
SSK	Single Skin Kite	
TE	Trailing Edge	
WT	Wind Turbine	

Symbol	Description	Units
A	Projected wing area	m^2
AR	Aspect Ratio	
b	Wing span	m
C	Coefficient	
D	Drag force	N
L	Lift force	N
S	Wing surface area	m^2
v	velocity	m/s

Greek symbol	Description	Units
α	Angle of attack	deg

Subscripts	Description	Units
∞	Free-stream	
τ	Tangential	
a	Apparent	
D	Drag	
d	Drag of airfoil	
D,i	Lift induced drag	
D,k	Drag of kite	
D,t	Drag of tether	
k	Kite	
L	Lift of kite	
l	Lift of airfoil	
LE	Leading Edge	
M	Moment of kite	
m	Moment of airfoil	
r	Radial	
t	Tether	
w	Wind	

List of Figures

List of Tables

1 Introduction

Airborne Wind Energy is a technology for harvesting wind energy using tethered flying devices. These can be both sailplane-like aircraft [3, 36] and flexible kites [51**?**]. The technology was already conceptualized during the oil-crises of the 70's and 80's [35, 45], but was shelved due to dropping oil prices and therefore less need for alternative sources of energy. With advances in material science and computing, the concept however was brought back to life by Wubbo Ockels. Nowadays there are more than 60 companies and institutions active in the field of Airborne Wind Energy [49]. There are two main ways available. The first uses a wing on a conducting tether and has the generators on the wing itself (see figure. 1.1 middle). The second one is called the yo-yo concept or ground-gen and is the focus of this thesis. This concept is used by Kitepower. It uses a wing (either flexible or rigid) that is connected to a ground-based generator through a tether. By flying figures-of-eight, high traction forces are created with which the tether is reeled of a drum, driving the generator. When the end of the tether is reached, the kite is tilted and reeled back in with much less force [11, 50]. This consumes a small fraction of the energy produced during reel-out. Different strategies exist for this retraction phase [22], however this is not part of this research.

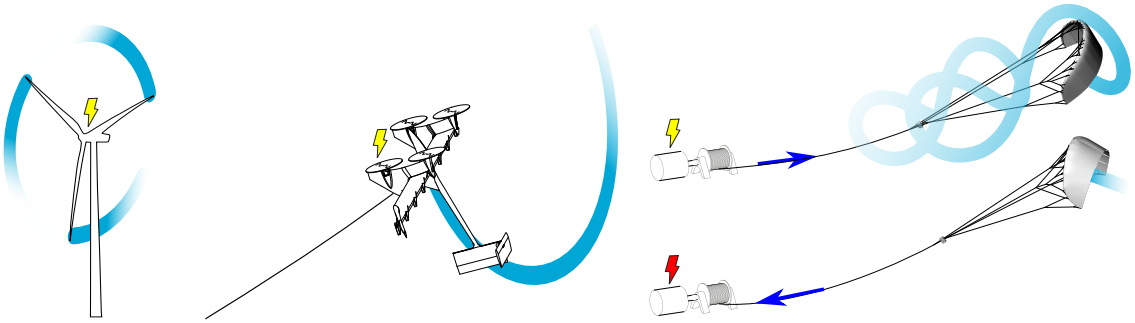

Figure 1.1: AWE power generating concepts with FlyGen in the middle and GroundGen or yoyo on the right

The main advantages of technology lie in the reduction of material usage compared to a conventional wind turbine (WT) and a lower wind speed where the rated power is produced. In a Horizontal Axis Wind Turbine (HAWT) the tower and blades are cantilever beams, which makes them relatively inefficient structures. This inefficiency is compensated with high material usage and a heavy concrete foundation. Furthermore the high speed parts (the tips) of the blades, produces most of the torque and therefore the most energy. An AWES replaces these large and inefficient structures with two things: a tether and intelligence. This eliminates up to 95% of the structural mass [20, 30]. The second advantage is that at higher altitudes the wind is more consistent, increasing capacity factors compared to HAWTs. Another advantage is that it can be used in deep water applications [12].

HAWT are limited in terms of water depth, but AWES can be put on a relatively small floating platform, making wind power available in waters that would normally not be suitable for wind energy harvesting.

Airborne Wind Energy was first described by Payne [45], but did not take off until Miles Loyd made the first prototype [35]. His power equation is the foundation for crosswind kite power and shows the system's potential.

$$P = \frac{2}{27}\rho S \frac{C_{\mathrm{L}}^3}{C_{\mathrm{D}}^2} v_{\mathrm{w}}^3 \tag{1.1}$$

In which ρ is the air density, S is the wing surface area, C_L is the lift coefficient,C_D is the drag coefficient and finally, v_w is the wind speed. However, there is a tether attached to the kite, which also experiences aerodynamic drag. This equation therefore needs tuning to take this into account. To account for the tether, a variation on the $C_{\mathrm{L}}^3/C_{\mathrm{D}}^2$ is introduced by means of equation 1.2.

$$C_{\mathrm{D}} = C_{\mathrm{D,k}} + C_{\mathrm{D,t}} \frac{d_t l_t}{4S} \tag{1.2}$$

Where $C_{\mathrm{D,k}}$ is the drag coefficient of the kite, $C_{\mathrm{D,t}}$ is the drag coefficient of the tether and the rest of the term is the normalization of the tether surface with wing surface. The 1/4-term is debatable and has been argued by Argatov [7], but in [8] he also mentions 0.31. It depends on the assumptions one can make on local tether velocity.

1.1. Kitepower

While flying a kite on the beach, Wubbo Ockels found the difference in traction force between a parked kite and one flying crosswind maneuvers remarkable. After some research he landed at the papers by Payne and Loyd [35, 45]. He then developed the idea for the Laddermill [40, 41]. In 2005 the Kitepower research group was founded, where a technology demonstrator was developed for flexible kites. In 2016 the company Kitepower was founded on the technology basis from the research group. The aim is to enter the market with a 100 kW flexible kite system in 2019. For this scale they are developing a new flexible wing to replace the old Leading Edge Inflatable (LEI) kitesurf kite. One of the concepts under investigation is a Single Skin Kite (SSK) (see figure 1.3, right). The system consists of three main components (see figure 1.2):

1. Groundstation/generator
2. Kite Control Unit (KCU), a pod under the kite that houses the autopilot and steering actuators for the kite.
3. Kite

The ground station is not part of this research, although it is an integral part of system scaling in AWE. Different companies in AWE have shown that the flying and ground segment of an AWES are highly interdependent and need to be sized together to achieve the best system. Some research even suggests that these subsystems need to be sized differently for different locations and therefore wind conditions [26].

1.2. Thesis Goal

Due to the highly non-linear nature of a flexible kite, simulations for both aerodynamics and structures are complex and computationally expensive. Most research conducted at TU Delft therefore focusses on the LEI kites and the associated fluid-structure interaction problems. This complexity and the fact that until recently kites were only used as a recreational tool, have led to kite design

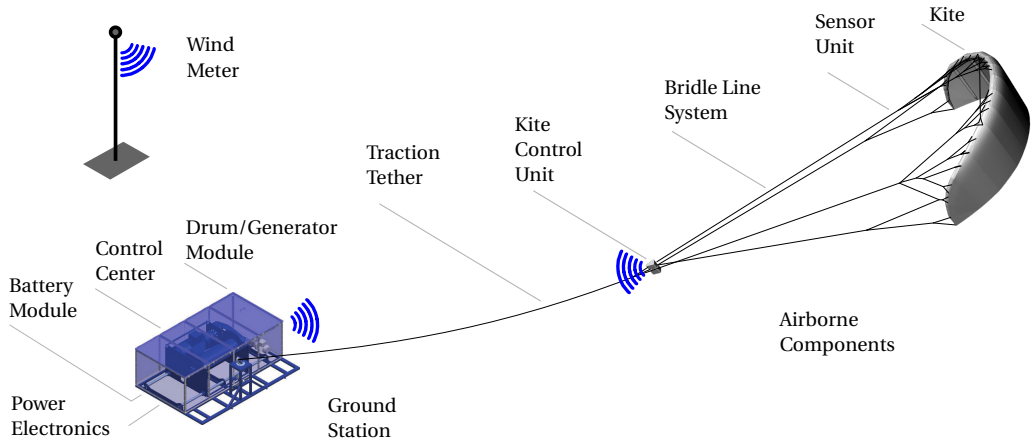

Figure 1.2: System components of Kitepower's 20 kW technology demonstrator

Figure 1.3: LEI kite from Kitepower (left) and Peak 2 Single Skin kite from Flysurfer (right) [31]

being mostly experience-based, and relied on rules of thumb and basic finite element models. On top of that, it also has been a mostly iterative process. This is because kites are relatively cheap and design by trial and error is therefore possible. Now however, with Kitepower's projected 75-100 m^2 wing area, this rapid prototyping strategy is not advisable anymore, both for size and performance requirements. Another disadvantage is scaling: LEI kites need more struts per span and thicker materials to take up the large forces associated with AWE, as well as an inherent problem that for equal internal pressure a thicker tube needs stronger/thicker walls which increases the weight. Therefore an aerodynamic study combined with optimization is proposed on the airfoil of a SSK to lay a basis for SSK design. This leads to the following research questions and objective:

Develop an airfoil for a single skin kite that maximizes traction power for a yoyo AWES, by means of CFD analysis and numerical optimization.

To answer this question, the following objectives will be evaluated.

1. Find an airfoil family/parametrization with a minimum number of design variables while keeping suitable variability and shape control.

2. Generate a high quality mesh, of which the process can be automated and no manual interference is required.

3. Can a steady-state RANS CFD solver be used for simulating a SSK airfoil?
4. Perform a sensitivity study on the SSK airfoil.
5. Derive a suitable objective function for AWES SSK airfoil optimization
6. Is surrogate modelling a suitable method for aerodynamic SSK airfoil optimization?

Where the choices for a steady-state RANS analysis and surrogate modelling are explained in chapters 2 and 3.

In chapter 2, the aerodynamic analysis is described. Previous research on kite aerodynamics is explored and a parametrization is presented. Next, one failed meshing strategy is presented and one successful, that will be used throughout the rest of the research. A mesh convergence study is performed as well as validation with wind tunnel data. Chapter 3 describes the optimization process and the different models used in the attempt to build a reliable model with a low number of objective function evaluations. In chapter 4, the results of the optimization are given and finally, chapter 5 holds the conclusions and recommendations for future research on this topic.

2

Aerodynamics

In this chapter, the methods for the aerodynamic analysis are described. First an overview on aerodynamics in previous work on kite aerodynamics is given. Next, the kite's flight envelope is identified, the aerodynamic model is explained, the meshing strategy is shown and the settings for OpenFOAM are given. A mesh convergence study is performed and finally validation of the solver is done on a standard NACA 2412 airfoil.

In figure 2.1 the airfoil definitions are shown. On the left side the definitions for the aerodynamic forces which, if one divides them by $1/2\rho V_\infty^2$ yield the aerodynamic coefficients used throughout the rest of the report. It is common for 2D or airfoil data to be designated with lower case letters and 3D or full wing coefficients with upper case letters. In this way, C_l is the section or airfoil lift coefficient and C_L is the wing lift coefficient. On the right side the airfoil terminology is given. The chord line is the straight line that connects the front of the wing, the Leading Edge (LE), to the back of the wing, the Trailing Edge (TE). The thickness is the difference between the top and bottom surface. The mean camber line is the line that equally divides the top and bottom surface. The distance between this and the chord line is called camber. Length scales on airfoils are always normalized by the chord length. In that way for instance thickness and camber are measured in percentages.

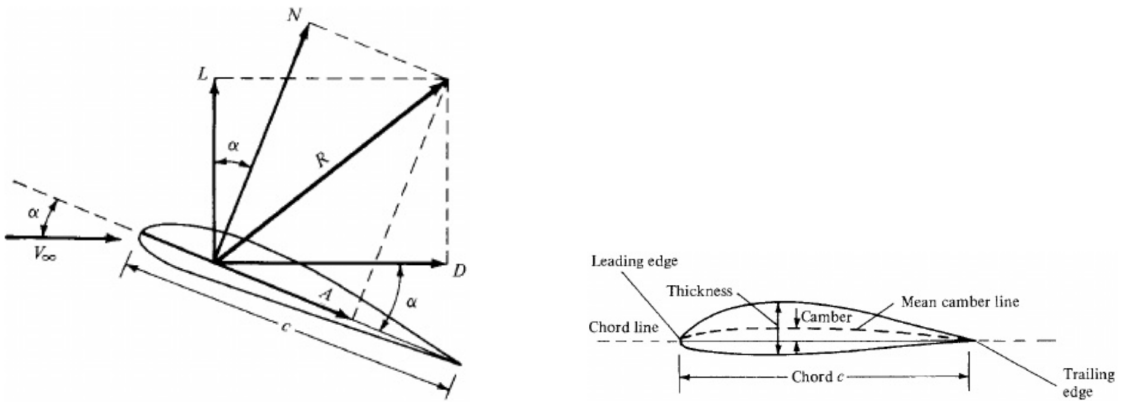

Figure 2.1: Airfoil nomenclature [5]

2.1. Previous work

Deaves [16] was the first to investigate a full LEI-kite using Reynolds Averaged Navier Stokes (RANS) CFD, as is also used in this work. He used Kitepower's V2 25m^2 kite. The complex flow phenomena

that surround a kite turned out to be difficult to simulate. There is always a region with detached flow, either behind the LE tube or on the upper surface. One big simplification was not to model the struts on the underside of the kite. Comparisons to [9] showed that the cross flow components of the flow due to the large anhedral angle (downward bending towards the tips), cannot be neglected. Leuthold [34] used a Vortex Lattice Method for the same kite. Multiple vortex shedding locations were induced to capture the detached flow. The result came within RANS-simulation confidence regions, with the limitation of small α's and only with small regions of separation. Paelinck [43] performed CFD on a SSK airfoil wing, where the wing was rigid, straight, low AR (5) and finite. Also the fluid domain was small. Results therefore have little physical meaning, since it is neither a 3D approximation for the actual kite, nor a proper 2D method. Dunker [19] gives design considerations for ram-air kite airfoils. He aims for $C_{\mathrm{l,max}}$ in his design. He suggests a relatively thick (14-16%) airfoil with its location of maximum thickness forward of the quarter chord. Paulig [44] focuses on ram kites as well. He focuses mainly on L/D and its specific impact on system handling and not so much traction power. In [38], an investigation is done into parawing airfoils. Both numerical/analytical and experimental analysis are performed. Especially the splitter plate case is interesting as a potential validation case. However, the experiments are not logged very clearly and for instance reference areas cannot be found, making it very hard to relate to this work. Venturato [55] performed an optimization for a rigid wing where he optimizes for $C_{\mathrm{L}}^3/C_{\mathrm{D}}^2$ while not accounting for a tether drag contribution.

Except for the work of Paelinck, no previous work has been done on single skin kite airfoils. This leaves a gap that this project will start to fill.

2.2. Flight envelope

The Reynolds number is a qualitative number that is the ratio between inertial and viscous forces of the flow [5]. It is defined as

$$Re = \frac{\rho_\infty V_\infty \bar{c}}{\mu} \tag{2.1}$$

In this ρ_∞ is the air density, V_∞ is the free stream flow velocity, or in the AWE case v_{a}, and $\bar{c}$ is the characteristic chord, or Mean Aerodynamic Chord. μ is the kinematic viscosity and has a value of $\mu = 1.581 \cdot 10^{-5}$. The MAC is defined as [2]:

$$\bar{c} = \frac{2}{S}\int_0^{\frac{b}{2}} c(y)^2 dy \tag{2.2}$$

Here, S is wing surface area, b is wing span, $c(y)$ is the chord length along the span and dy is the span coordinate over which $c(y)$ is integrated.

Leuthold proposes a Re-range of $3.3 \cdot 10^6 > Re > 8.1 \cdot 10^6$ [34] for the 25 m^2 kite, however if upscaling is taken into account and a lower operating altitude than the given maximum of $h = 1000$ m, the range would be $8 \cdot 10^6 > Re > 20 \cdot 10^6$. This is based on characteristic chord of 6m and velocities of 20 to 40 m/s. Unfortunately this is not a range of Re where a lot of experimental data is available. For soft or membrane wings the Re's are usually a lot smaller. For rigid wings, the target Re is usually higher, but tests are done at lower Re due to wind tunnels allowing limited size models (and therefore restricted $\bar{c}$). This leaves us with a gap that can probably only be filled by test flights [42] or CFD simulations. Currently, the University of Berlin is running tests on kitesurf kites in a controlled environment to determine their aerodynamic performance [47].

The average velocity of 30 m/s is lower than the $M = 0.3$, or 0.3 times the speed of sound. In this range the fluid can be regarded as incompressible. This simplifies the Navier-Stokes equations as presented in section 2.4.

2.3. Potential flow methods

Potential flow is a theory that describes the velocity field around an object moving through a liquid. This theory is based on a linearization of the equations presented in section 2.4 [5]. This theory has proven to be very useful for airfoil design. Its limits are that some flow-phenomena cannot be captured and can only be used in specific conditions: non-rotational and non-viscous flow. By coupling the potential flow solution to a set of viscous boundary layer equations, one can approximate reality quite well. This leads to a powerful design and optimization tool since the methods are fast and computationally inexpensive, like Xfoil [18] and MSES [17]. For this work, these properties sound perfect. However, the fact that potential flow is not able to capture rotational flow, strong gradients and boundary layer separation make it unsuitable. Under the airfoil a vortex-field can be expected (see figure 4.1) and immediate flow detachment at x/c_{bot}. Let alone the points of maximum power, which are expected to be close to α_{stall}. This leads us to use a computationally more expensive method as described in the next section.

2.4. Navier-Stokes equations

The full set of equations for aerodynamic analysis are called the Navier-Stokes equations [5]. They are given in Einstein notation in equations 2.3-2.4.

$$\frac{\partial u_i}{\partial t} + u_j \frac{\partial u_i}{\partial x_j} = -\frac{1}{\rho}\frac{\partial p}{\partial x_i} + \nu \frac{\partial^2 u_i}{\partial x_j^2} \tag{2.3}$$

$$\frac{\partial u_i}{\partial x_i} = 0 \tag{2.4}$$

Where x denotes the spatial location, u is the flow velocity and i is the subscript for the three spatial dimensions (so x, y and z). ρ is the density, p is pressure and ν is the kinematic viscosity. Together this set of non-linear set of partial differential equations describes the flow properties for incompressible Newtonian flow at constant temperature. The full set includes temperature as well and an extra equation for conservation of energy, but that equation is not necessary for incompressible flows. Equation 2.3 describes the conservation of momentum through the domain. Equation 2.4 describes the conservation of mass.

Solving for all flow fluctuations does not make sense from an engineering point of view, as described in further detail by [16]. Therefore a Reynolds Averaged Navier-Stokes (RANS) method is used. This method divides the flow properties in a mean and time dependant, fluctuating component, as given for the velocity in equation 2.5.

$$u(t) = \bar{u} + u' \tag{2.5}$$

Using this, the NS equations reduce to:

$$\overline{u_j}\frac{\partial \overline{u_i}}{\partial x_j} = -\frac{1}{\rho}\frac{\partial \overline{p}}{\partial x_i} + \frac{1}{\rho}\frac{\partial}{\partial x_j}\left(\mu \frac{\partial \overline{u_i}}{\partial x_j} - \rho \overline{u_i' u_j'}\right) \tag{2.6}$$

$$\frac{\partial \overline{u_i}}{x_i} = 0 \tag{2.7}$$

The fluctuating terms function as an increase in viscosity would. It adds to dissipation of kinetic energy. They are known as Reynolds Stresses and need to be modelled seperately. This is described in section 2.5.

This non-linear set of differential equations cannot be solved analytically. Hence one needs to discretize them and solve them numerically. The discretization of the space around the airfoil is called meshing and its result a mesh. This process is described in Sections 2.7 and 2.8.

2.5. Turbulence Modelling

To solve the problem of the Reynolds Stresses, one needs to add a turbulence model to the RANS-equations. Frequently used models include Prandtl's mixing length model [46], Spalart-Allmares [52], $k-\epsilon$ [33], and $k-\omega$ [59]. In this simulation however Menter's Shear Stress Transport (SST) model, is used [39]. This model has shown good results for airfoil flow and combines the strengths of both $k-\epsilon$ and $k-\omega$ models. It is based on the Boussinesq eddy viscosity postulation [4] that replaces the $\rho\overline{u_i' u_j'}$-term by replacing it with an effective viscosity term, ν_t for momentum transfer of small eddies. In the inner part of the boundary layer, approximately up to 0.5δ, or half the boundary layer thickness, is modelled by the $k-\omega$ model. A blending function then blends the $k-\omega$ with the $k-\epsilon$ model for the outer parts of the boundary layer and the free-stream. This is done because the $k-\omega$ is highly dependant on free-stream flow values and the $k-\epsilon$ model does not perform well near walls. In this way it exploits the strong points of both models. A flow transition model could be implemented but is not deemed necessary in this work. The Re and α's are assumed large enough that the transition to a turbulent BL happens on or very close to the LE. Also, the real-world kite has seams and rough cloth along the leading edge, which promote transition.

2.6. Airfoil

For the airfoil a modified NACA 4-digit airfoil [2] was chosen. The airfoil is fully defined with 5 parameters by itself and one is added for the length of the bottom skin, making a total of six design variables. The airfoil was chosen to keep the number of optimization variables reasonable as the evaluation is computationally expensive. The parameters are:

1. Maximum camber ($c_{\max}$)
2. Location of maximum camber ($x/c_{\mathrm{c,max}}$)
3. Maximum thickness ($t/c_{\max}$)
4. LE radius, where 6 defines the radius for a standard NACA 4-digit airfoil (LE_{rad})
5. Location of maximum thickness ($x/c_{\mathrm{t/c,max}}$)
6. Location of (x/c_{bot}) (Added)

This airfoil is given by a set of polynomials. The coefficients for these are given by the parameters above, which are approximated in [15] to give the function for these coefficients. In this way, the coefficients do not have to be derived for each airfoil separately. Where the top of the airfoil is defined by two polynomials, as is the original, the bottom is only defined by one, namely the one that extends from LE to $t/c_{\max}$. In this, then the $t/c_{\max}$ is replaced by x/c_{bot} to enforce the boundary condition of being horizontal at this point.

In this way, a 2412-63-2 airfoil has 2% maximum camber, at 40% chord and with 12% maximum thickness. The LE radius is 6, which is not a physical parameter but one that defines the polynomial leading coefficient, maximum thickness location at 30% chord and a bottom surface that extends up to 20% chord. This then looks like figure 2.2. A list of coordinates can be found in appendix A.

2.7. Mesh

Two meshing strategies were attempted. The first was with *blockMesh*, which was chosen for the sake of simplicity. The second strategy was hyperbolic extrusion of a closed airfoil and filling with unstructured cells. The latter proved to be successful.

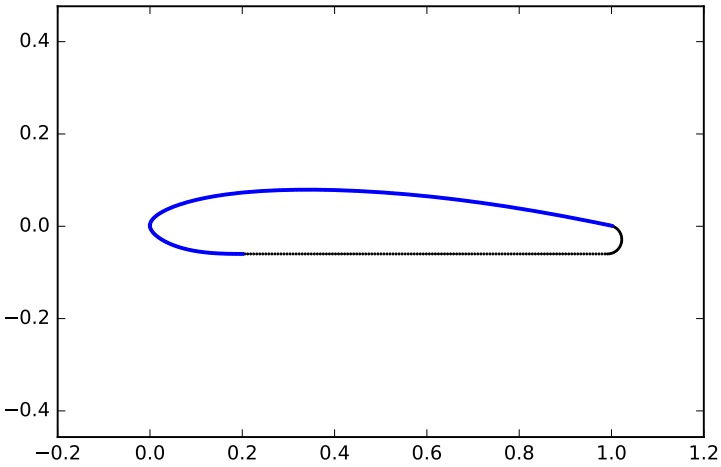

Figure 2.2: Basic airfoil with closing line and arc (dotted)

2.7.1. blockMesh

In an attempt to keep complexity down it was first chosen to use the OpenFOAM built-in functionality *blockMesh* [27]. In a blocking strategy the domain is divided in sections called blocks. The blocks can be assigned cell distributions along each edge as long as the cell distribution on the boundary between neighbouring blocks is the the same. Blocks can also have curved edges. The domain was divided in three main sections containing a number of blocks: far-field, near-field and inside the airfoil. The airfoil itself had a finite thickness. The blocking diagram is depicted in figure 2.3. The strategy proved to provide insufficient control in a number of places. At the boundaries of the far-field LE-block, the cells were very stretched, but at the next block they were not. The trailing cells of the finite thickness airfoil did not match the boundary layer cells coming from the surface and a number of similar problems arose which were unable to be overcome. A different strategy was therefore chosen.

2.7.2. Hyperbolic extrusion

The next attempt, it was chosen to use hyperbolic extrusion because of the high quality mesh that can be achieved. It builds "layers" around the airfoil, with the added capability that through smoothing iterations, convex surfaces can also be accomodated without the crossing of mesh lines. The program *Overture* (v26) [10, 28] was used. To be able to use this easily, the airfoil is closed with a straight line on the bottom surface and a closing arc at the TE, as shown in figure 2.2. This line is then splined by *Overture* with 3 attractor points on the spline. These attractor points make sure that in regions of high gradients the mesh is refined. They are placed at the LE, TE and x/c_{bot}. The nodes are then extruded outward up to the far-field boundary and inward by $0.01c$. These two domains are stitched with *OpenFOAM*'s functions *mergeMesh* and *stitchMesh* along the line and arc sections. The inner domain is then filled with unstructured hexahedra with the open source program *gmsh*(v3.0.3) [24]. The resulting mesh is shown in figure 2.5. The settings for *Overture* are given in table 2.1. The airfoil is of infinitesimal thickness since only the cell faces on the airfoil are closed and there is no closed surface/volume. The O-grid is specifically suitable for this application: In a C-grid one would remesh for every α to have the wake as much in the direction of the flow as possible. In the O-grid this is equal for all α's. Although remeshing does not take long compared to computing time, every meshing process creates an opportunity for errors. The number of volume smoothing iterations is relatively low. The settings for the in- and outward extrusion needed to be

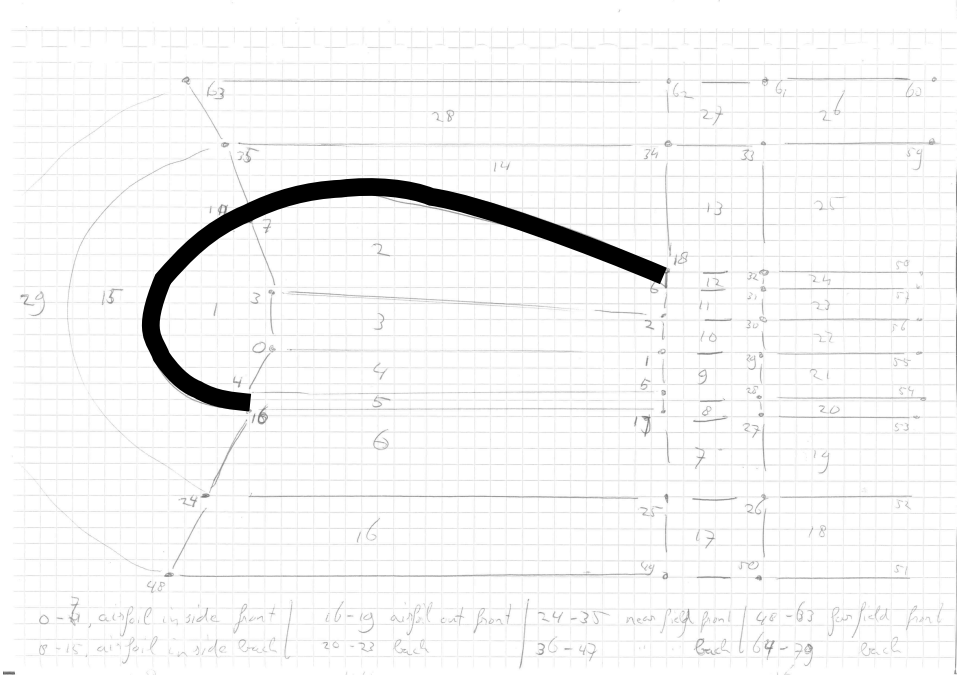

Figure 2.3: Sketch of attempted block and numbering strategy for *blockMesh*

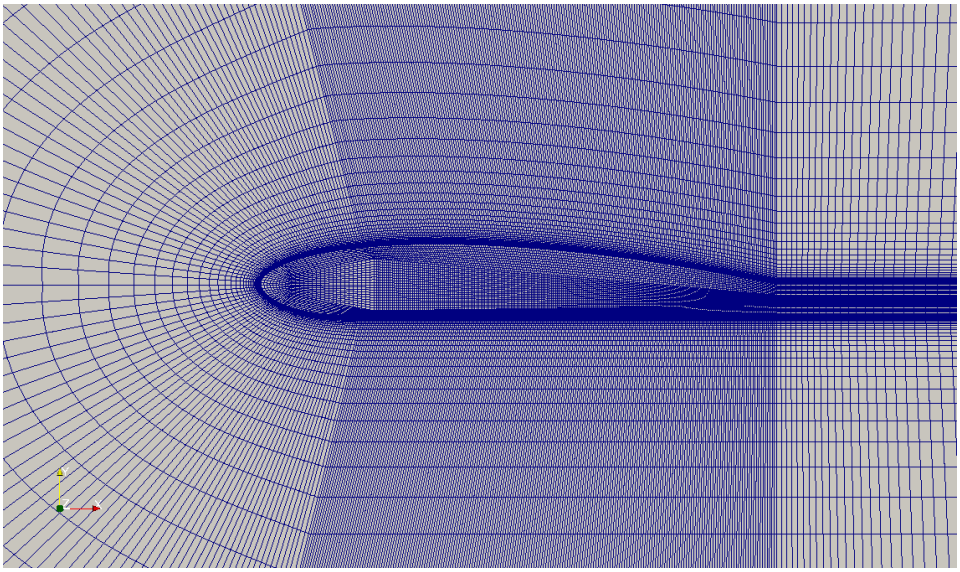

Figure 2.4: Mesh result for *blockMesh*

equal and a higher number of smoothing iterations resulted in negative cells on the LE and TE inner boundaries of the inward extrusion. Because of this, the higher cell density at x/c_{bot} almost reaches the far-field boundary (as seen in the top left picture in figure 2.5) instead of being smoothed out. This is not believed to have an effect on the overall calculations.

The mesh size is defined from here on as:

$$N_{\text{a}} \times N_{\text{r}} \tag{2.8}$$

Where N_{a} is the number of points on the airfoil spline and N_{r} is the number of chords that the domain extends radially from the airfoil.

Table 2.1: Overture meshing settings

Parameter	**Value**
Attractor point 1	20
Attractor point 2	20
Attractor point 3	20
Geometric stretching coefficient	1.2
Implicit coefficient	2.0
Volume smoothing iterations	500
Uniform dissipation coefficient	0
BC's	Periodic

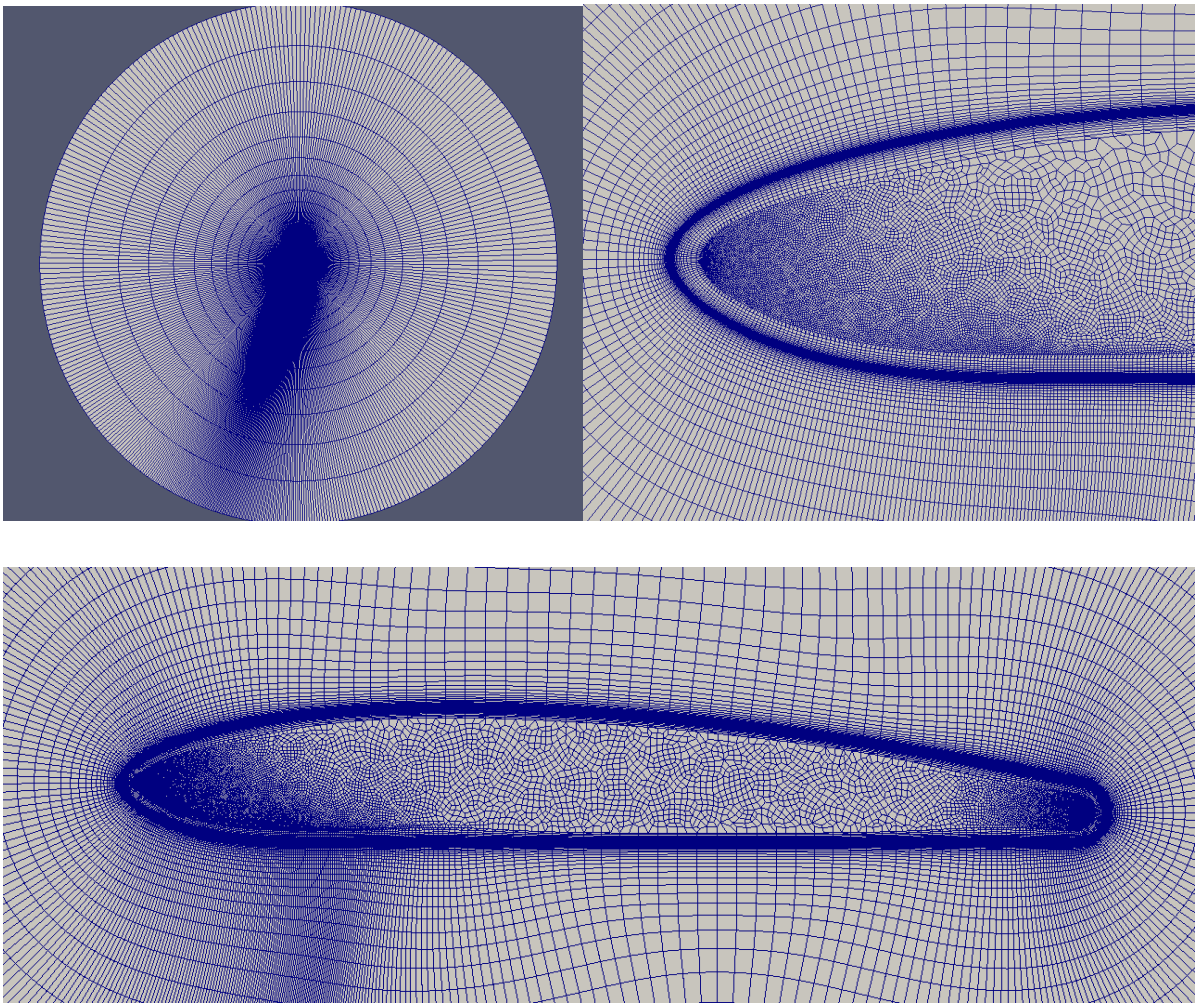

Figure 2.5: Mesh layout with far-field (top left), LE detail (top right) and airfoil close-up (bottom)

2.7.3. First cell size

The first cell size, that is the cell attached to a closed surface or wall, needs to have a dimensionless parameter $y^+ = 1$. This y^+ makes sure that the BL can be sufficiently resolved. y^+ is defined as:

$$y^+ \equiv \frac{u_* y}{\nu} \tag{2.9}$$

$$u^* \equiv \sqrt{\frac{\tau_w}{\rho}} \tag{2.10}$$

Where u^* is the friction velocity, y is the distance to the nearest wall and ν is the local kinematic viscosity. τ_w is the wall shear stress and ρ is the density. A decent first approximation can be made by substituting u^* with U_∞ and ν with ν_∞, which then needs to be checked and possibly refined in the meshing study (see section 2.9).

2.8. OpenFOAM

OpenFOAM is an open-source CFD program [58]. It uses the Finite Volume Method, which is a way to solve the NS-equations numerically in a discretized space or mesh, as described in section 2.7. It assumes the values to be constant throughout the cell and calculates the flow parameters with fluxes through the cell faces. The outflow of one cell should be the inflow of the next. This method is well suited for unstructured meshes, which is also OpenFOAM's strong point. The structured mesh is actually saved in an unstructured way.

2.8.1. simpleFOAM

simpleFOAM is an *OpenFOAM* solver for the incompressible RANS-equations as presented in equations 2.6 and 2.7. SIMPLE stands for Semi-Implicit Method for Pressure-Linked Equations [56]. In particular, *OpenFOAM* is set to the SIMPLE-c or SIMPLE-consistent algorithm, in which the momentum equation is modified compared to the SIMPLE-algorithm. One particular benefit is that it allows for higher under-relaxation factors than standard SIMPLE, while remaining stable. simpleFOAM has an option to use a non-orthogonal corrector step. This can be used if the mesh is not optimal in places. However a very good mesh-quality was achieved using the hyperbolic extrusion so this is not necessary. It does not improve the solution and only adds computation time.
The simpleFOAM algorithm works as follows:

1. Make initial guess
2. Solve discretized momentum equations
3. Solve pressure correction equation
4. Correct pressure and velocities
5. Solve other discretized transport equations
6. Set values as new initial guess
7. Iterate 1-6 until convergence

Table 2.2: Relaxation factors and residual control

Variable	**Relaxation factor**	**Residualcontrol**
p	0.99	1e-6
U	0.99	1e-6
k	0.99	1e-6
omega	0.95	1e-6

2.8.2. Schemes

In table 2.3, the discretization schemes for OpenFOAM are given.

Table 2.3: Discretization schemes for OpenFOAM

Term	Scheme	
ddt	steadyState	
gradSchemes	Gauss linear	
divSchemes	ϕ, U	bounded Gauss linearUpwind
	ϕ, k	bounded Gauss upwind
	ϕ, omega	bounded Gauss upwind
	nuEff*dev2(T(grad(U))	Gauss linear
laplacianSchemes	Gauss linear corrected	
interpolationSchemes	linear	
snGradSchemes	corrected	
fluxRequired	default no; p	
wallDist	meshWave	

2.8.3. Boundary Conditions

In stead of using the real-world values, non-dimensional versions will be used. The Re was already established in section 2.2 to be $Re = 14 \cdot 10^6$. U and c are taken to be 1.
k, or the turbulent kinetic energy, is calculated with:

$$k = \frac{3}{2}(U \cdot I)^2 \tag{2.11}$$

Where U is the velocity and I is the turbulence intensity as a percentage of U.
ω, the specific dissipation, is calculated with:

$$\omega = \frac{k \cdot \frac{\mu_t}{\mu}}{\nu} \tag{2.12}$$

Where k is the turbulent kinetic energy, μ_t/μ is the turbulent eddy viscosity ratio and ν is the kinematic viscosity. The farfield boundary conditions are listed in table 2.4. The airfoil BC's are given in table 2.5.

Table 2.4: Farfield boundary conditions for OpenFOAM

Variable	Value
U	1
p	0
k	$3.75 \cdot 10^{-3}$
ω	$5.25 \cdot 10^4$
ν_t	0
ν	$7.14 \cdot 10^{-8}$

By default OpenFOAM requires a three-dimensional mesh. This being a investigation into two-dimensional flow, however, only two directions are required. This is done by setting front and back-faces of the domain to an *empty* boundary condition. By defining these as *empty, OpenFOAM* does not solve the equations in this direction, yielding a 2D solution. One would use a wall function when the mesh does not provide $y^+ <= 1$. This is not the case here. It used because *OpenFOAM* detects the first cell size and only switches the wall function on if necessary. Wall functions are approximations of the boundary layer in case the mesh is not sufficiently refined to capture its behaviour properly.

Table 2.5: Airfoil boundary conditions for OpenFOAM

Variable	Value
U	0
p	zeroGradient
k	0
ω	omegaWallFunction
ν_t	0
ν	$7.14 \cdot 10^{-8}$

2.9. Mesh convergence

A mesh convergence study was performed, to see where the solution reaches sufficient mesh independence. The number of cells around the airfoil, the domain size and the first cell size are tested.

2.9.1. Cells around airfoil

The number of cells around the airfoil proved to be relatively large. In the end 400 cells, together with the attractor points mentioned in section 2.7, proved to be sufficient. This number is high compared to a 'normal' airfoil where 200 is already quite a lot. This is due to the complex flowfield behind the LE with two counter-rotating vortices, high turbulence intensity and free shear layers. In figure 2.6, it is shown that between 200, 300 and 400 cells, the drag changes dramatically where the lower number of cells is also not able to capture a drop in C_d after $\alpha = 5°$. Between 400 and 500 however, the lift and drag only change by 0.85% and 1.21%,respectively, with a 25% increase in number of cells. This can be seen in figure 2.7 and table 2.6. It should be noted that this difference is based on the differences between the values and not compared to the windtunnel data from figure 2.9. These values are higher since they were run at the proposed $Re = 14 \cdot 10^6$ from section 2.2. Since the drag is not the driving optimization factor, as explained in section 4.2, the 400 cells are considered to give a sufficiently mesh-independent solution.
For the convergence criterion on the residuals a value of $1 \cdot 10^{-6}$ was used. If one then looks at the C_l and C_d history throughout the iterations, as being the parameters of interest, one can see that they already stop changing before the residuals reach the convergence threshold. $1 \cdot 10^{-6}$ is therefore considered to be a sufficiently low criterion. The C_l and C_d history throughout a 400×500 simulation can be seen in figure 2.7.
NB At first, the mesh only had attractor points (as described in section 2.7) on the LE and TE. The region of high gradients at x/c_{bot} however made the mesh convergence nearly impossible: at 600 cells there was still no real sign of mesh-independence.

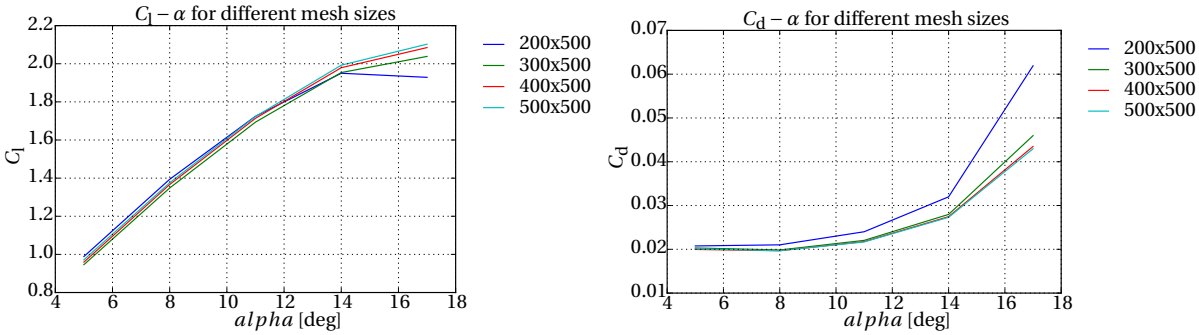

Figure 2.6: C_l (left) and C_d (right) curves for the mesh convergence study

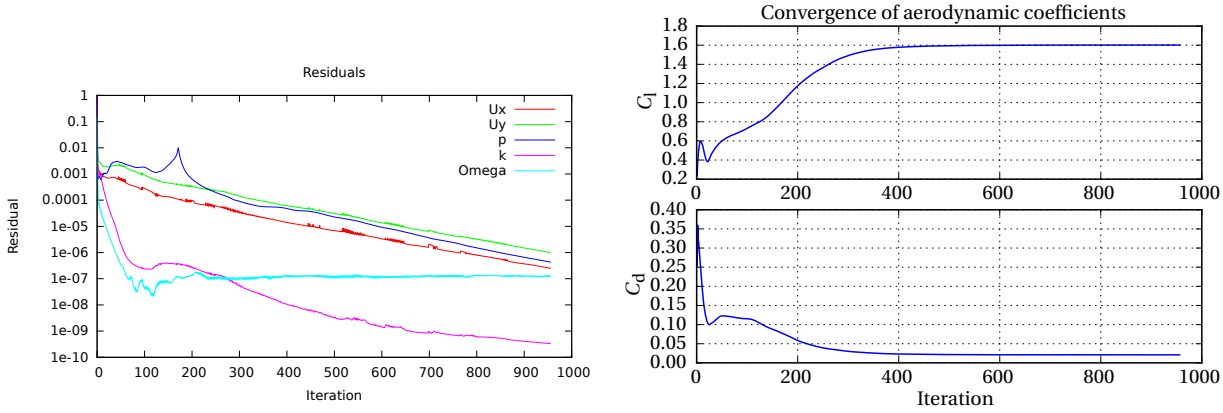

Figure 2.7: Residual convergence history (left), C_l (top right) and C_d (bottom right) history throughout the simulation for 400×500

Table 2.6: Relative maximum lift and drag difference on airfoil

Mesh size	$\mathbf{C_l}$	$\Delta\mathbf{C_l}$[%]	$\mathbf{C_d}$	$\Delta\mathbf{C_d}$[%]
200×500	1.92869	-	0.06191	-
300×500	2.03841	5.68	0.04596	-25.76
400×500	2.08484	2.27	0.04349	-5.37
500×500	2.1026	0.85	0.04296	-1.21

2.9.2. Domain size

The first simulations were performed with $N_r = 50$. This domain size proved to produce inconsistent results and poor convergence. At $N_r = 100$ the simulations produced better results. As a test, then $N_r = 500$ was also tested. This showed no change in the values given in figure 2.6, but the time for each α to converge went down dramatically, by more than 1/3. The huge domain however came only with a 10% cell number penalty. This can be attributed to the way the cells grow radially by a constant growth factor in the extrusion process. The reason for the faster convergence can be attributed to the fact that disturbances from the airfoil have already died out before they hit the farfield boundary [48]. *OpenFoam* therefore does not have to try to numerically enforce boundary conditions. In figure 2.8, it can be seen that the turbulence that enters the domain indeed dissipates before it hits the airfoil. Also, the disturbances generated by the airfoil do not reach the far field boundary.

2.9.3. Initial value

For the initial values a uniform flowfield was assumed for both p and u_i, with u_i in the direction of α. To create a more realistic initial flowfield, it was tried to use the solver potentialFOAM. As the name suggests it solves potential flow equations and is often used as a primer for more advanced solvers to limit computation time of the computationally more expensive solver. Due to the complex nature of the flow, as described in section 4.1 and the reason why potential flow methods were not an option in the first place, convergence of the simulation was slowed down. As potential flow does not contain vortices, the 'virtual' airfoil is not captured and the flow that follows the underside of the airfoil now reverses into the LE section and follows the surface to the TE. As a primer, or otherwise, this is useless.

2.9.4. First cell height

As described in section 2.7.3, the first cell size was estimated using the mean free stream inflow values. This can also be attributed to the smoothing process which stretches and compresses the

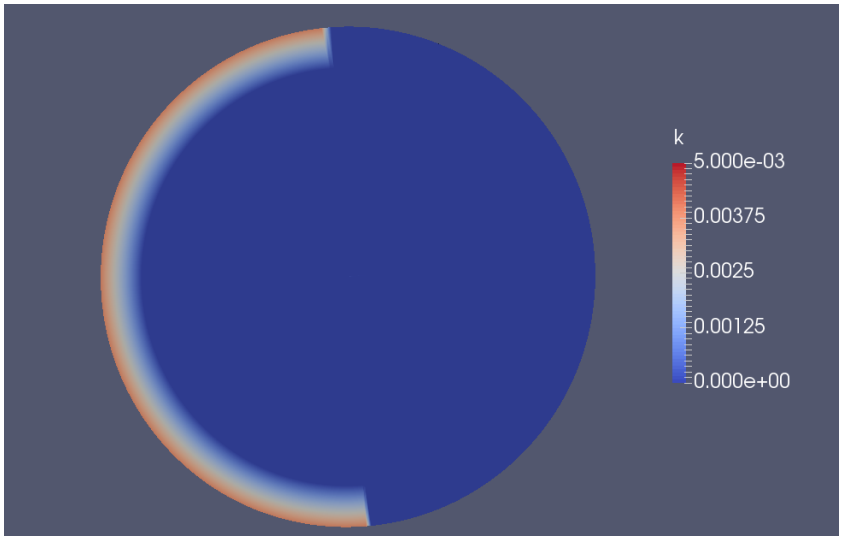

Figure 2.8: Turbulence intensity k for 2412-63-2 airfoil at $\alpha = 5°$

cells close to the boundary. However the flow around the airfoil accelerates, especially at high angles of attack, which is as shown in the next section. This is also the region of interest for the optimization and therefore the initial cell height was halved, to keep the BL properly resolved. The new first cell height is h =2.5 $\cdot 10^{-6}$ m.

2.10. Validation

The performance of the methods (both mesh and solver) is assessed by comparison of a standard NACA 2412 airfoil to windtunnel experiments. The NACA 2412 was chosen because it is also the basis airfoil that is used for the sensitivity study of section 4.2. The same settings for Overture were used for the outward extrusion. The domain radius presented in section 2.9.2 is used for this airfoil as well. The calculations are compared to wind tunnel experiments from [2] at $Re = 9.0 \cdot 10^6$. The results for different numbers of N_a are shown in figure 2.9.

The C_l's correspond quite well to the experiments and only deviate a few percentage points. After stall the CFD solution deviates more. α_{stall} is predicted relatively well. De C_l predictions do not vary much as N_a is increased. The C_d is systematically over-predicted with a maximum of 37%. Close to stall, the predictions match the experiments better, though. This may be due to that the experiments having less laminar flow and coming closer to a fully turbulent flow. The C_l matches quite well. Not only the lift slope but the $C_{l,max}$ as well. With increasing cell count the C_l predictions do not vary and $C_{l,max}$ keeps being underpredicted. This systematic error is acceptable in the sense that the real optimum airfoil can be identified, but the power factor or resulting $C_{l,max}$ might be off.

2.11. Process summary

The full process of aerodynamic analysis can be seen in figure 2.10. x is the design vector which holds the design variables described in section 2.6. The airfoil and mesh are generated. The mesh is checked for quality metrics like negative volumes, cell-to-cell volume ratio and aspect ratio. The cell aspect ratio check allways fails due to the mesh being quasi-3D. The BL cells are very thin but relatively long in z-direction. If the mesh is invalid or when the process times out, the airfoil is rejected. Time-out can happen when for instance *Overture* or *gmsh* produce a faulty mesh and therefore do not exit properly. Next, simpleFoam is started using all available processors. For each α, the results are collected and written to a single log file that holds the aerodynamic properties,

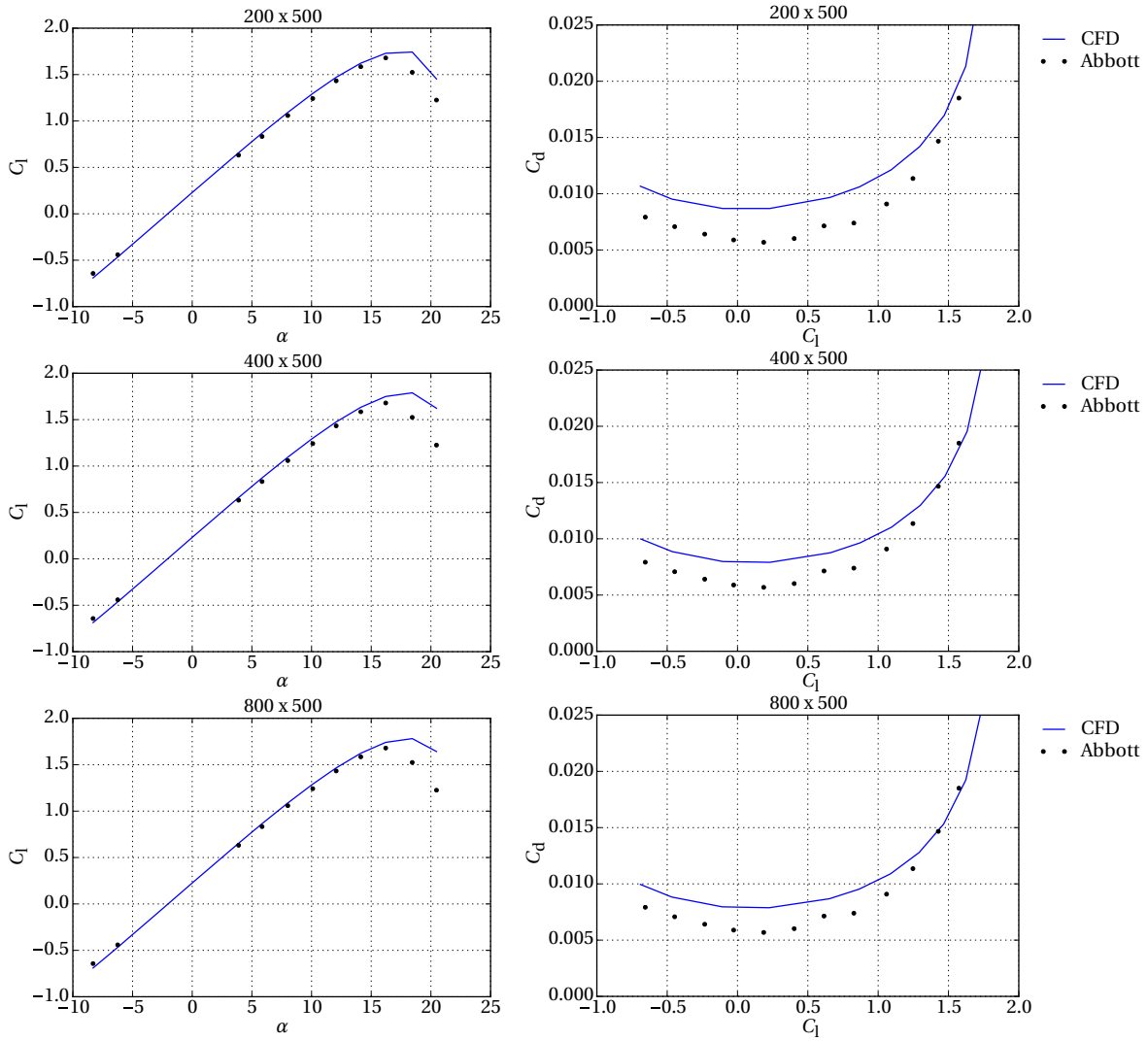

Figure 2.9: Windtunnel comparisons for a standard NACA 2412 airfoil with C_l on the left and C_d on the right

number of iterations and if it is considered converged at $iter_{max} = 3500$. If from these results only four or less α's have converged, the airfoil is removed from the results due to what are considered to be too large gaps in between data points. Then it is tested of the maximum value of the objective function is found on the boundary of the range of α's. If so, another run is started, broadening the α search range. Finally, the maximum objective function is returned to the SUMO-toolbox. Erroneous results are given a $Obj = NaN$ result, which are discarded by SUMO.

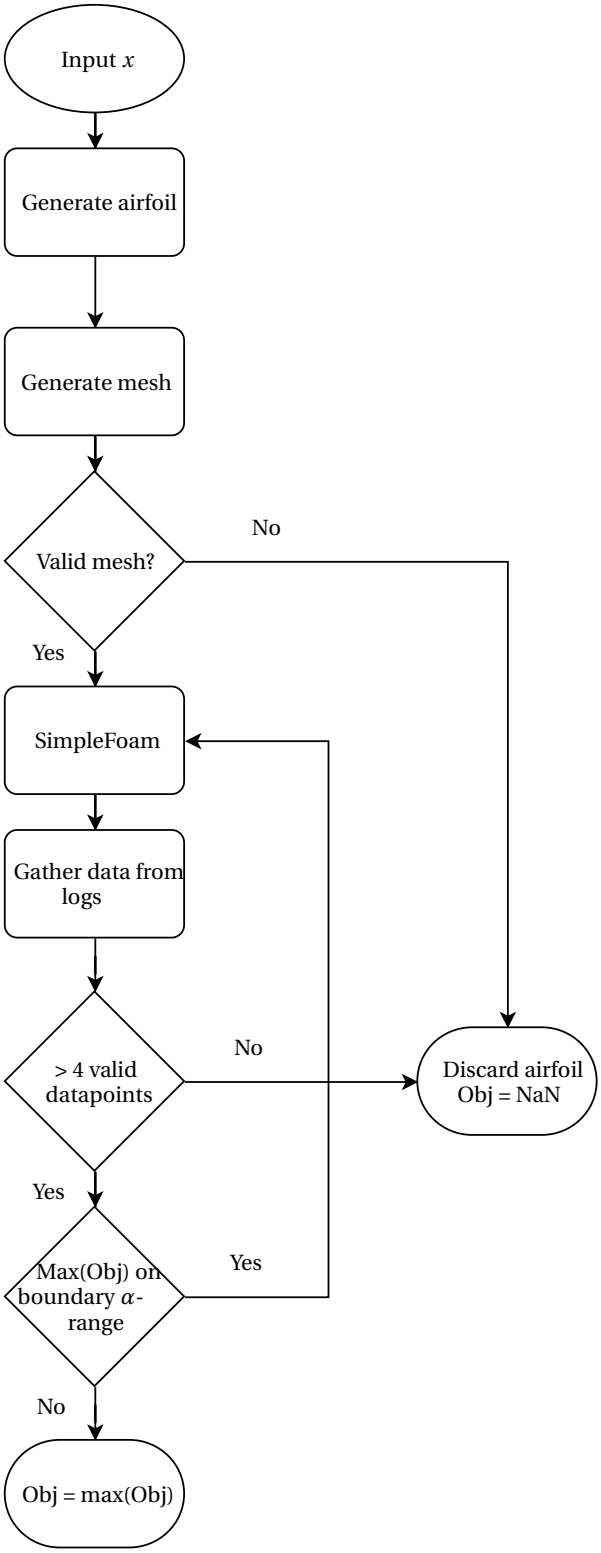

Figure 2.10: Flowchart for the aerodynamic analysis process

3

Optimization

In this chapter the optimization process for the SSK airfoil is addressed. First, other optimization methods will be briefly explained in sections 3.1 and 3.2 and why they are not used. Secondly the SUMO-toolbox, SM process and subprocesses are explained and finally the search space bounds and settings are given.

Optimization means minimization (or negative maximization) of some function $f(x)$, which is also called the objective function or cost function [6].

$$\begin{aligned} &\min f(x) \\ &\underline{x} \in \mathbb{R}^n \end{aligned} \tag{3.1}$$

Possibly, but not necessarily under constraints

$$\text{subject to } g(\underline{x}) \leq 0\,;\ \underline{g} \in \mathbb{R}^m,\ m < n \tag{3.2}$$

In a typical airfoil design exercise such an optimization would be to minimize C_d at a certain C_l. This can possibly be augmented with constraints on C_m or minimum thickness to leave room for the wing structure.

In equation 1.1, the instantaneous power of a cross-wind flying, massless kite was given. From this, the term $C_\mathrm{L}^3/C_\mathrm{D}^2$ represents the kite's performance. This will be used here as the function to optimize:

$$\min f(X) = \min\left(-\frac{C_\mathrm{L}^3}{C_\mathrm{D,eff}^2}\right)\left(c_\mathrm{max}, x/c_\mathrm{c,max}, t/c_\mathrm{max}, LE_\mathrm{rad}, x/c_\mathrm{t/c,max}, x/c_\mathrm{bot}\right) \tag{3.3}$$

These coefficients however, are for a 3D kite, while in this work, there will only be 2D simulations. Therefore an approximation of a full kite is required. This was made using conventional wing theory [5]. The C_L is approximated with:

$$C_\mathrm{L}{}^* \approx \frac{C_\mathrm{l}}{1+\left(\frac{C_\mathrm{l}}{\pi ARe}\right)} \tag{3.4}$$

Where AR is the aspect ratio and e is the Oswald span efficiency factor. This is a measure of how close the lift distribution approximates an optimal elliptical lift distribution. The wing drag is given by the airfoil drag coefficient and the lift-induced drag:

$$C_\mathrm{D} \approx C_\mathrm{d} + \frac{(C_\mathrm{L}{}^*)^2}{\pi ARe} \tag{3.5}$$

For the actual 3D lift approximation the $C_L{}^*$ is multiplied by the projected wing area over actual wing surface area, to account for the large anhedral angle. Not all the kite's wing surface is pointing directly in the direction of the tether tension. The projected area is the area on the ground plane when the kite is in loaded shape.

$$C_L = \frac{A}{S} \cdot C_L{}^* \tag{3.6}$$

The values used for this approximation are given in table 3.1. These are not believed to change significantly when designs for the SSK mature.

Table 3.1: Assumed values for 3D lift and drag approximation

Parameter	**Value**	**unit**
AR	5.05	-
e	0.7	-
A/S	0.742	-

3.1. Iterative methods

Iterative optimization methods are generally fast and guarantee finding the optimum value. However these, as the name suggests, usually require a lot of function evaluations to gain enough information of the problem. They just try to see if they find a better function evaluation, without exploiting knowledge like gradients.

3.2. Heuristics

A smarter way is to use information given by the system to determine a search direction and in more advanced way also step sizes. This is used in gradient based methods, where the local gradient is indicative of the direction in which a minimum lies and therefore the search direction. These methods rely on a relatively large amount of function evaluations, because around a sample point, multiple other points need evaluation to get the local gradient. Gradient-based methods can also get trapped by local minima and therefore need guidance like random multi-start to get to a global optimum.
A more recent, and popular, way of optimization is the Genetic Algorithm (GA). It populates the design space with a random selection of evaluations and picks the best performing samples to "breed" and reproduce. Usually some degree of randomization or mutation is performed on the next "generation" to not only be captured by local minima. These require a lot of function evaluations as well since there is still a degree of randomization involved.

3.3. Response Surface Methods

A special sub-category of heuristics are Response Surface Methods (RSM) or Surrogate Modelling (SM). These are used when design variables in the problem do not have a well defined correlation with the objective function, or a correlation which is not known yet. They are also especially useful in situations where the problem takes a long time to evaluate [21]. The subject of this thesis is such a problem. RSM fits a model to objective function evaluation points or samples. It can be viewed as an intelligent form of interpolation. This model can then be optimized with less complex methods, like described above. What really makes RSM interesting, also for other applications, is that the full design space is covered. One can use the same data for different objectives or one can use the model for control or machine learning purposes. The power lies in sequential design [13]. The process looks as follows:

1. Design of Experiment

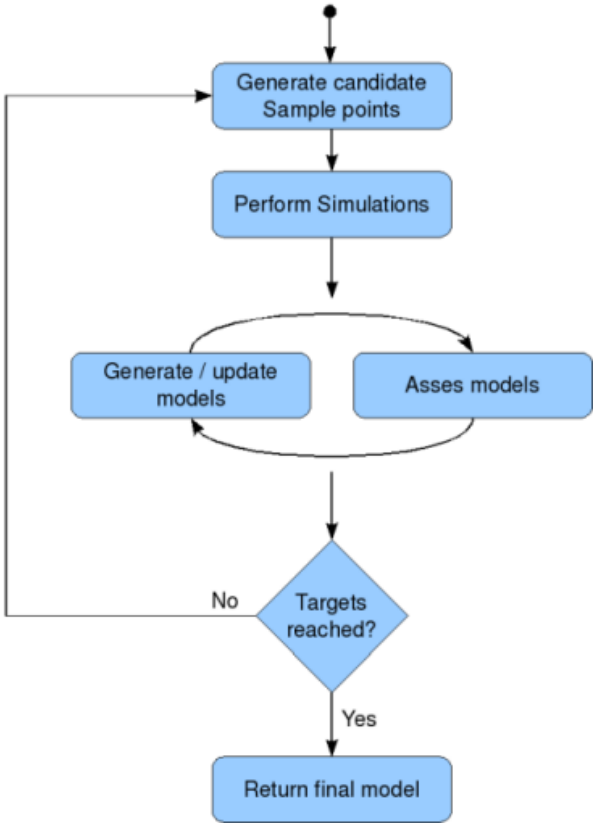

Figure 3.1: SUMO process [1]

2. Fill sample space
3. Build SM
4. Get best decision x_n
5. Evaluate x_n
6. Add x_n to sample space
7. Start from (3) for $N_s = N_s + 1$ until N_{it} or improvement threshold is reached
8. Get global optimum

Where x_n is the next sample decision, N_s is the number of samples in the sample space and N_{it} is a pre-set number of extra decisions. First, a batch of samples is evaluated, this is called the Design of Experiment, because these points are determined beforehand. After that, the sequential design phase starts. In this phase samples are chosen based on information from the model. These choices have to be balanced between two qualities: exploration and exploitation. Exploration means that one would like to build an accurate model over the entire design space. By this, one will not miss regions of interest like local minima or non-linear regions, because they were not sampled. Exploitation means that one would like to build an accurate model close to the global optimum. Just like gradient-descent methods it uses information to obtain samples near the optimum, without much care for the rest of the domain. For the implementation the SUMO toolbox in *Matlab* is used [25]. An example of the resulting model for a 2D problem can be found in figure 4.9, where the surface is the model built by the toolbox and the dots are the samples.

For an entire SM optimization one needs 5 algorithms: DOE, modelling, sequential design, error estimation and final model optimization. These models will be explained in the next sections. From [54] it appeared that a low number of sample evaluations may suffice. In this case, from figure 4.7 the problem appears to be smooth. Therefore the number of samples is set to $10n = 10 \cdot 6 = 60$. Also, the LOLA-Voronoi sequential design strategy and Kriging model builder appeared to be scoring very well overall. Therefore these algorithms shall be employed here as well. They are described in the next sections. To reduce the number of α evaluations of the airfoil, the range given in section 3.4 is only evaluated in between $\alpha = 13^\circ$ and $\alpha = 18^\circ$. The results are interpolated with a spline around the maximum point. When the maximum is on the bounds of the initial search space, extra α's are evaluated. The maximum for that airfoil is then found using Matlab's *fminsearch*, which will then be the objective function value for this airfoil.

3.3.1. Latin Hypercube DOE

In the design of experiment the initial sample batch is generated, without prior knowledge of the behaviour of the objective function. The most simple ways are to use a uniform distribution and Monte Carlo sampling [37, 57]. A uniform distribution is found through dividing the sample space in equal parts. This means that every variable range is divided into equal parts and one just obtains a grid. This grid however repeats variables. In this way, not the maximum amount of information is obtained from the underlying model. Monte Carlo sampling is done by using a random number generator with uniform distribution to generate the samples. With low sample numbers, there is however the danger of bunching, which is having the samples close together and not covering the full design space. Latin hypercube designs are usually pre-generated. They are optimized on criteria like prediction variance, with simulated annealing or minimum potential energy. These methods try to ensure that all samples are as evenly distributed over the design space as possible [23, 57].

3.3.2. Kriging

Kriging is a form of stochastic regression. There are different forms, assuming more or less information and exploiting more or less [29]. Here the *corrmatern32* correlation function is used. A nice feature about the stochastic nature is that is also gives a prediction variance over the domain. This can be seen as a validation error or trust in a certain region.

3.3.3. LOLA-Voronoi

For the sequential design strategy, the LOLA-Voronoi algorithm is used [14]. It is a hybrid between two algorithms: LOcal Linear Approximations (LOLA) for exploitation and Voronoi tesselation for exploration. The LOLA algorithm estimates the local gradient $\nabla f(x)$ to identify areas of interest in the design space. For the methods described in section 3.2, this would be done by running the simulator, but since were are dealing with an expensive function, that is not an option. The gradients are therefore estimated from the SM. The samples are divided in neighbourhoods. This can be considered to be a piece of the design space that is bounded by samples. In these neighbourhoods, candidate points are generated and checked if the samples provide information about them. At this point still only the location of the points is used and not the score. Neighbourhoods that score bad are preferred over "good" neighbourhoods. This is the Voronoi part of the sequential design. Next the actual gradients are approximated and the non-linearity of the regions are assessed. The two scores, so one score from LOLA and one from Voronoi, are combined into one score. The most undersampled region will then be sampled again. Undersampled in this case means either: too little samples, (locally) low sample density or non-linear regions.

3.3.4. Cross-validation

One needs a metric to score the models that are built with the Kriging after each new sampling iteration. K-fold cross-validation [32] is very common in machine learning and SM. Cross-validation means that the samples itself are used as validation data. However, because the modelling is a fancy version of interpolation, the model error in the actual samples is zero by definition. This is where the k-fold part comes in. The samples are divided in k folds, ie. 1/k. Which each in turn are left out. There are some ways to distribute the left-out samples, but the default in SUMO is uniform. This means the 1/k samples are distributed uniformly over the design space. The fold term is confusing in that the sample space is not really "folded" in k, because this would leave large gaps where the prediction error will always be very large. In the next step the 1-(1/k), i.e. the rest, of the samples are used to build a model. This happens k times, since each fold is left out, which results in k models. The predictions of these models are then compared to the validation data in the fold. The errors are scored and the model that performs the best, based on some error metric (in this case Root Mean Square Error), is saved and used for the next iteration of the sequential design.

3.4. Bounds

The optimization should be bounded inside a search space: not all airfoils make sense to evaluate. The bounds are defined on one hand by the limitations of the method of generating airfoils and meshing, on the other hand they are bounded by practicality. A design space that is too large will take more function evaluations to cover. The bounds are given in table 3.2. Next to practicality, the results of the sensitivity study of Section 4.2 support the choice of design variable range. One parameter choice that is not supported by the results in figure 4.7, is the lower bound on x/c_{bot}. This choice was made due to airfoil definition bounds. At $x/c_{\text{bot}} < 0.1$ the defining polynomials have trouble creating a smooth bottom surface.

Table 3.2: Bounds of the design space

Parameter	Lower bound	Upper bound
c_{max}	0	5
$x/c_{\text{c,max}}$	0	5
t/c_{max}	9	20
LE_{rad}	5	8
$x/c_{\text{t/c,max}}$	1	5
x/c_{bot}	1	5

3.5. Validation

Although in section 3.3.4 it is described that model selection is done with the same data as with which it is built, a validation set will be evaluated. This will be done with 4 randomly generated airfoils, plus the predicted optimum. Although validation usually refers to real-life experiments like wind tunnel testing, in this case the expensive black box function that is the CFD simulation, is considered to be the experiment.

4

Results

In this chapter, the results of the sensitivity and the optimization are presented. First, the flow characteristics around the 2412-63-2 base airfoil are shown in section 4.1. The results from the sensitivity study are given. Section 4.3 presents a surrogate modelling run using two out of 6 variables and finally the optimization with the full set is given.

4.1. Flow characteristics basic airfoil

In figure 4.1 the flow around the basic airfoil at 4 angles of attack is shown. The flow under/inside the airfoil forms a vortex field with two counter-rotating vortices of which the back one is driven by the external flow and the one inside the semi-closed section of the LE is driven by the former. This represents a lid-driven cavity flow of sorts. At large α's and smaller x/c_{bot}, these two merge into one vortex as the space for this gets smaller. The two slow-moving vortices have a higher pressure, so the external flow moves around it. In this way, these create a virtual airfoil, as can be seen in figure 4.2, where the streamlines from upwind follow the outside of the vortices. The double vortex is in contrast with Sylvestri [53], who tested a similar airfoil, but shows a single vortex, even at low α. Paelinck's simulations [43] do show a double vortex. At higher α the vortex region reduces to a single vortex. Graphs for k and ω can be found in appendix B.

In figure 4.3, the pressure distributions for the same α's as in figure 4.1 are given. Both lines are plotted from x/c_{bot} to LE to TE. One goes around the outside of the airfoil and one on the inside. In the outside surface line there is a wiggle around $x/c = 0.2$. The fact that this is consistent, has the same shape and is in the same location for each α, leads to believe that it is not due to any flow-related phenomena. It was checked if the problem was mesh related, but this was also not the case. In other pressure distributions, like in figure 4.17 it was not found either. The top-surface pressure distribution looks similar to a standard airfoil. The difference can be discerned on the inside surface. In the vortex region, the pressure is constant, which is to be expected. The pressure then rises towards where the flow coming from the x/c_{bot} reattaches. This pressure peak at the back leads to high pitching moment coefficients. It is also good to see that the inside and outside surface pressure match at x/c_{bot}, since this shows continuity in the pressure.

4.2. Sensitivity study

To get a feeling for the behaviour of the different airfoil parameters, they were independently varied between 0.5 and 1.5 times their original value. The starting point was the NACA 2412-63-2 airfoil. All airfoils were then evaluated between $\alpha = 5.0 - 20.0°$. These resulting C_{l} and C_{d} were then evaluated for $C_{\text{L}}^3/C_{\text{D,eff}}^2$ and $C_{\text{l,max}}$.

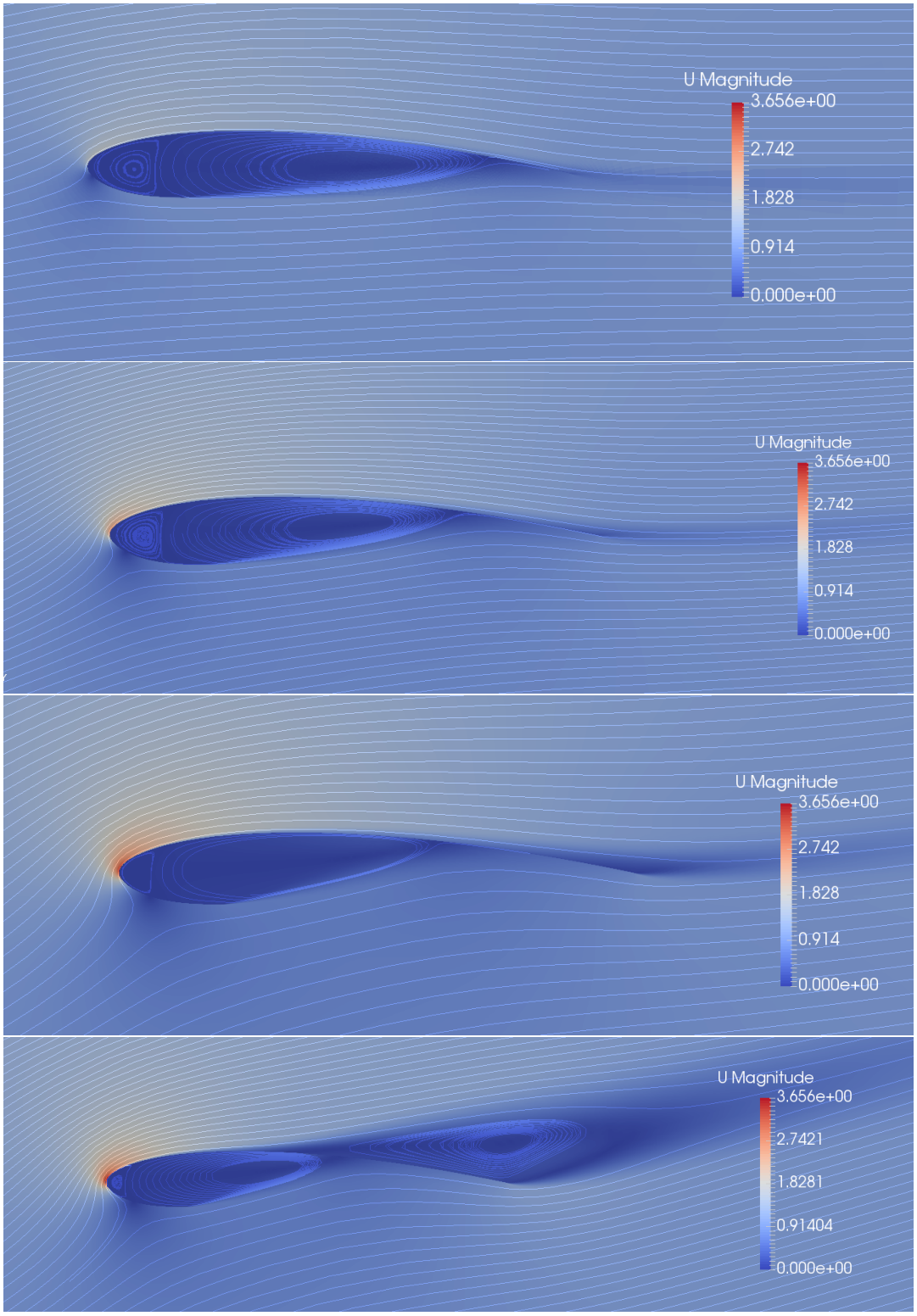

Figure 4.1: Streamlines for 2412-63-2 from top to bottom at $\alpha = 5°$, $\alpha = 10°$, $\alpha = 15°$ and $\alpha = 20°$, respectively

Different performance parameters were assessed in the preliminary batch-run. All 6 design parameters were varied independently between 0.5 and 1.5 times their basic value, giving 66 different airfoils. This gave insight into the effect of the change of the variables. Although dependency be-

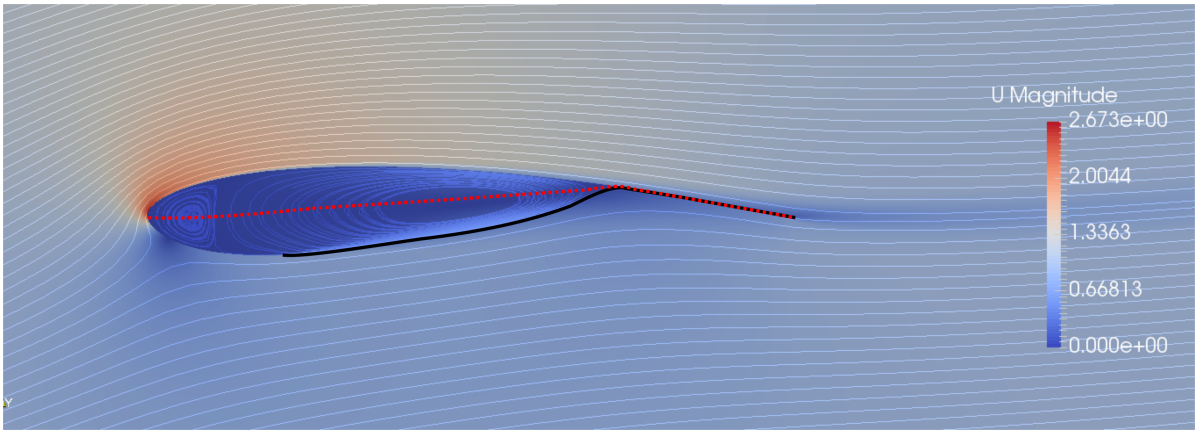

Figure 4.2: Virtual airfoil effect, with outer skin in black and camberline in dotted red

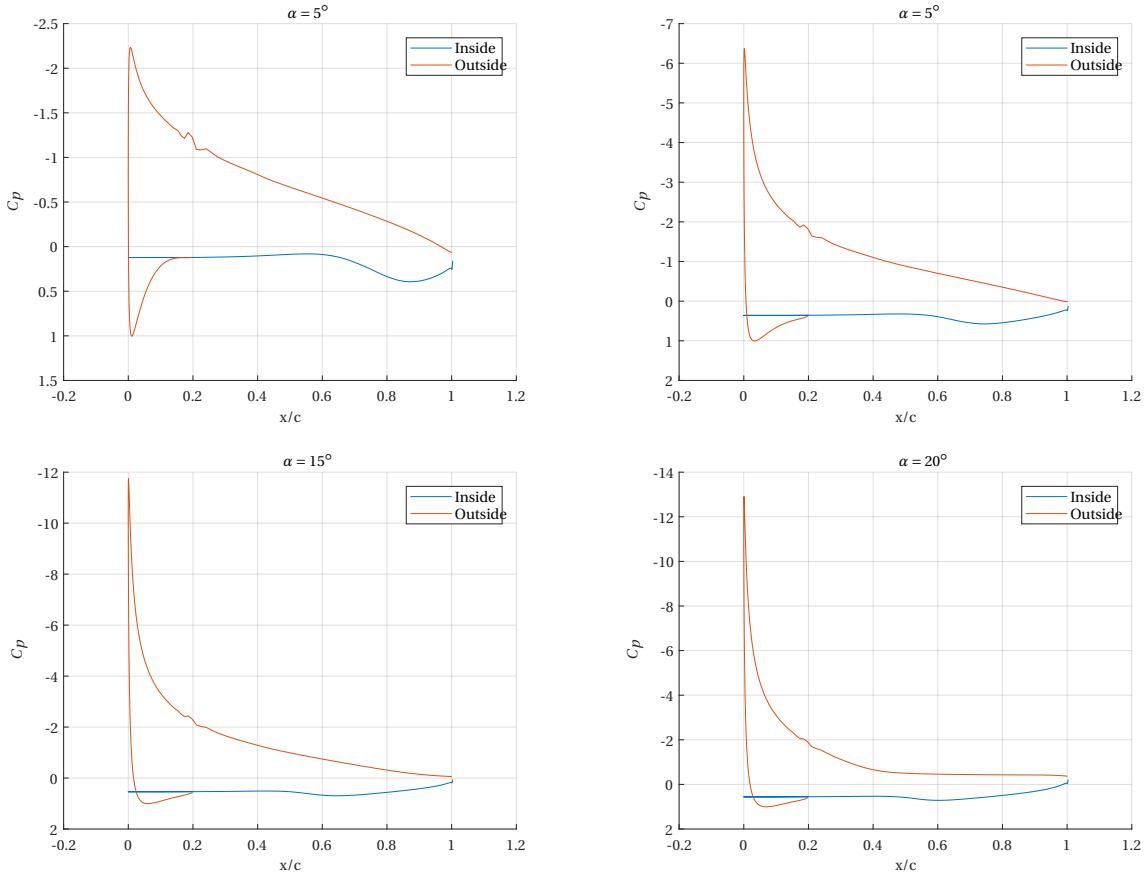

Figure 4.3: C_p-curves for the α's presented in figure 4.1

tween variables cannot be judged, because only one variable was changed at a time, a general insight into the behaviour can be deducted. Between the performance indicators under investigation three stood out to be of significant importance: $C_{l,max}$, $C_L^3/C_{D,eff}^2$, α_{opt}. These are the maximum lift coefficient, a 3D approximation of Loyd's power factor as described at the start of chapter 3 and the α at which this happens. They are presented in figures 4.6-4.8.

In figures 4.4 and 4.5, all C_l and C_d curves for the different airfoils are given. First it should be noted that the camber produces some outliers in both low and high ranges. They are split per

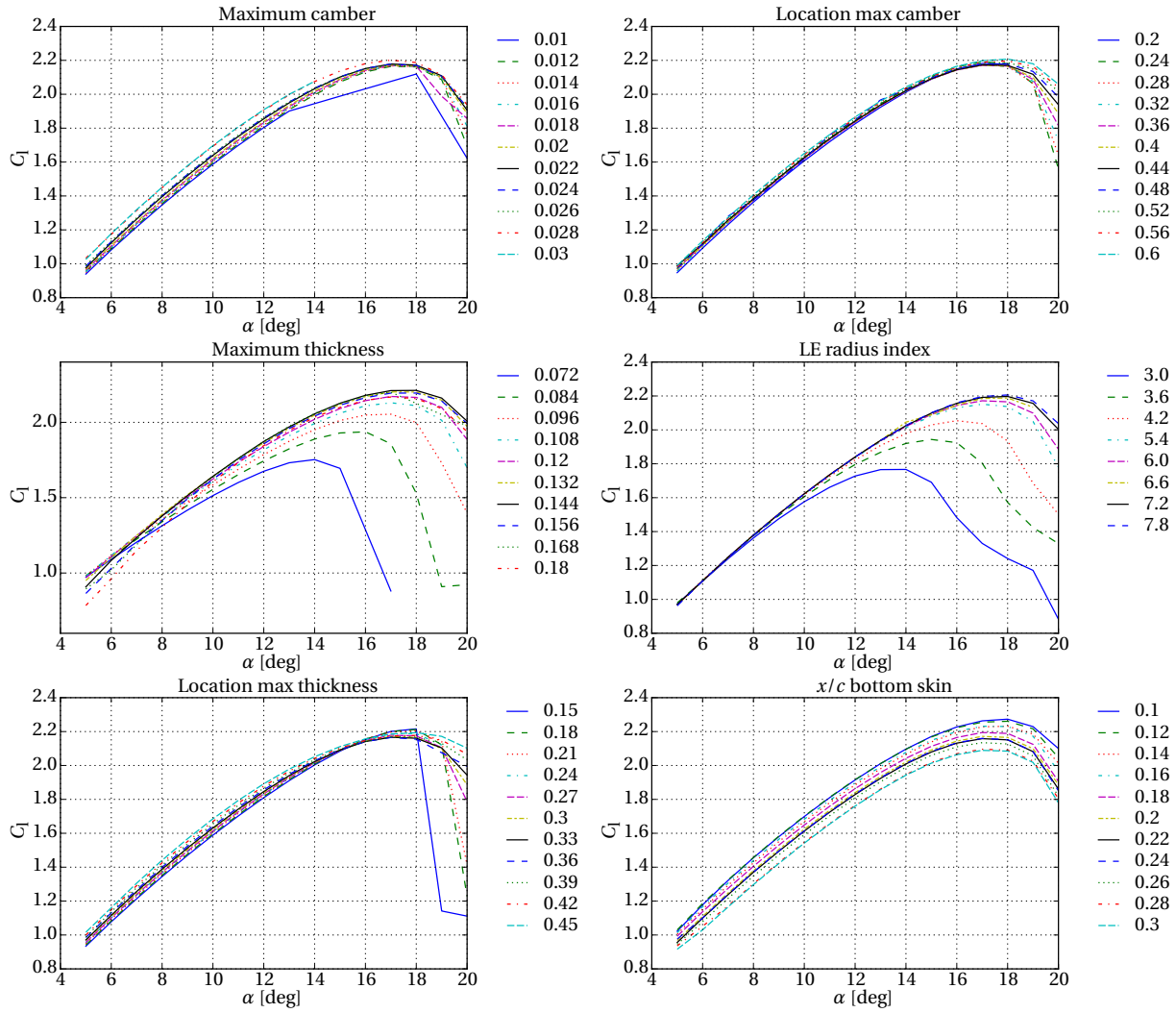

Figure 4.4: $C_l - \alpha$-curves for different design parameters in the airfoil naming order

parameter. What immediately stands out is that some parameters almost have no effect on the respective curves. For the C_l, camber (except the outliers), its location and the location of maximum thickness do not affect its behaviour very much. x/c_{bot}, LE_{rad} and t/c_{max} affect the C_l heavily, especially in stall or near stall regions. This can also be seen in conventional airfoils. The reason that the first three parameters have little influence is that the virtual camber line is almost independent of these variables. The C_d is much more influenced. Only camber location does not show an effect. Important to note is that one cannot deduct that certain parameters can be neglected in the optimization. This would be highly desirable to reduce design variables and therefore runtime, but since no correlation between the variables is investigated, one might miss information.

Compared to conventional airfoils, the $C_{l,max}$ behaves quite similar. A thinner LE and higher t/c_{max} both lead to a lower stall angle. If the location of maximum thickness is more forward the $C_{l,max}$ increases but remains relatively constant at more backward locations. What clearly stood out was the effect of x/c_{bot}. A shorter underside of the airfoil clearly leads to an increase in $C_{l,max}$. One explanation for the effect can be sought in the fact that the virtual camber line starts to curve upward earlier, creating a more cambered airfoil than defined in the variables. This can also be seen in the almost negligible impact of the camberline definition on $C_{l,max}$. The power factor follows the exact trend that $C_{l,max}$ is following. The angle of attack at which this happens shows that a maximum in PF

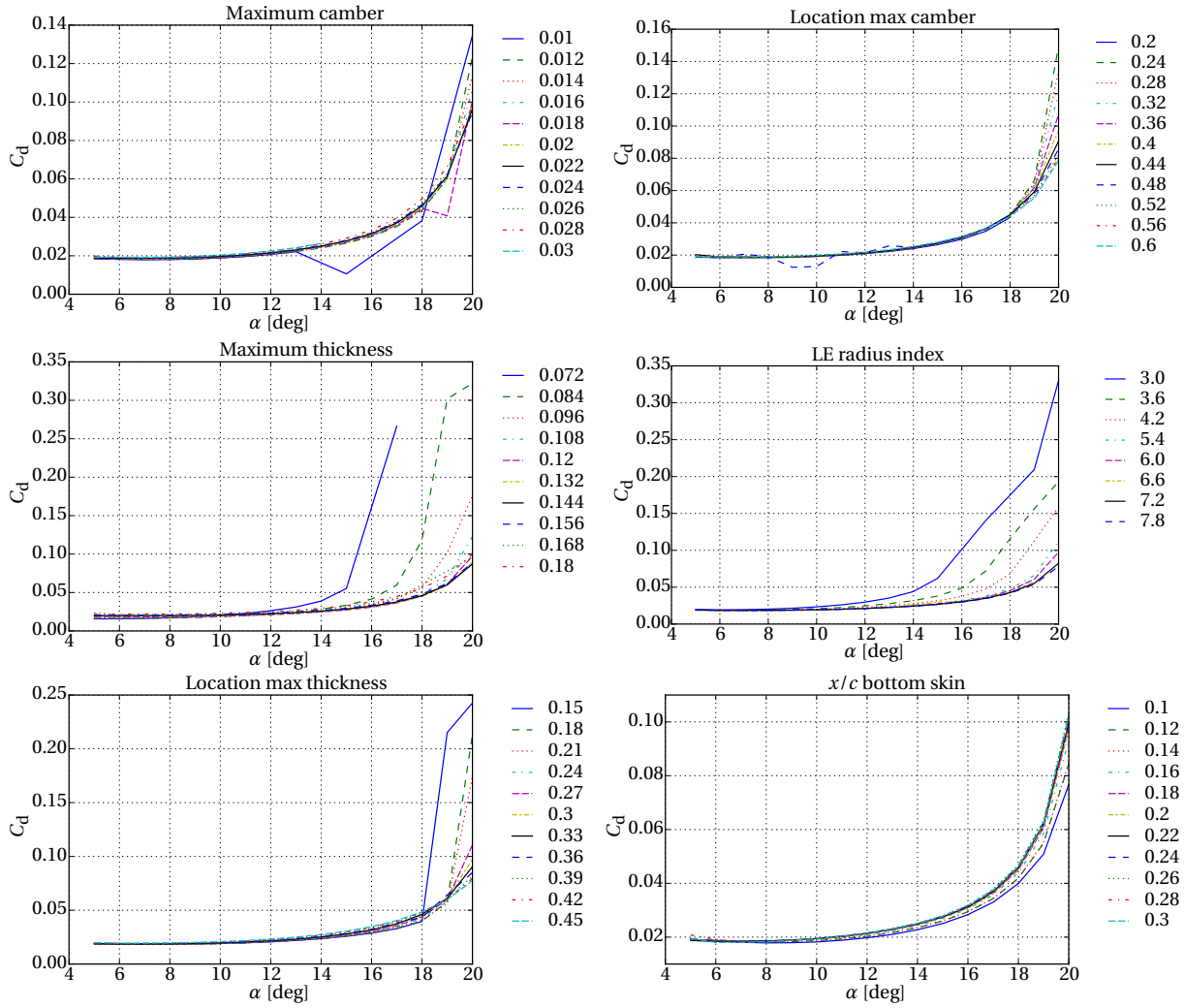

Figure 4.5: $C_d - \alpha$-curves for different design parameters

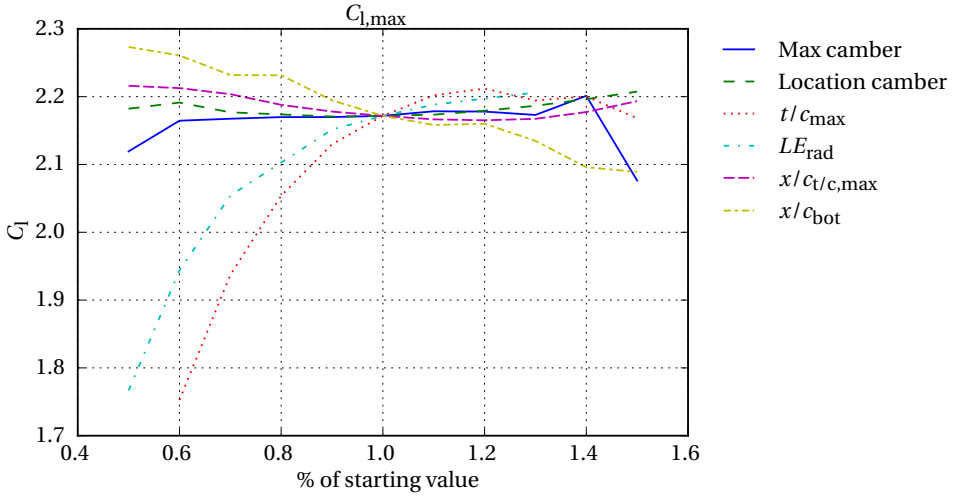

Figure 4.6: $C_{l,max}$ as a function of the design variables

is reached júst before α_{stall}. At this point, C_l is almost at its maximum but the airfoil has not reached the sharp increase in C_d that comes with stall yet. From an optimization standpoint it is therefore

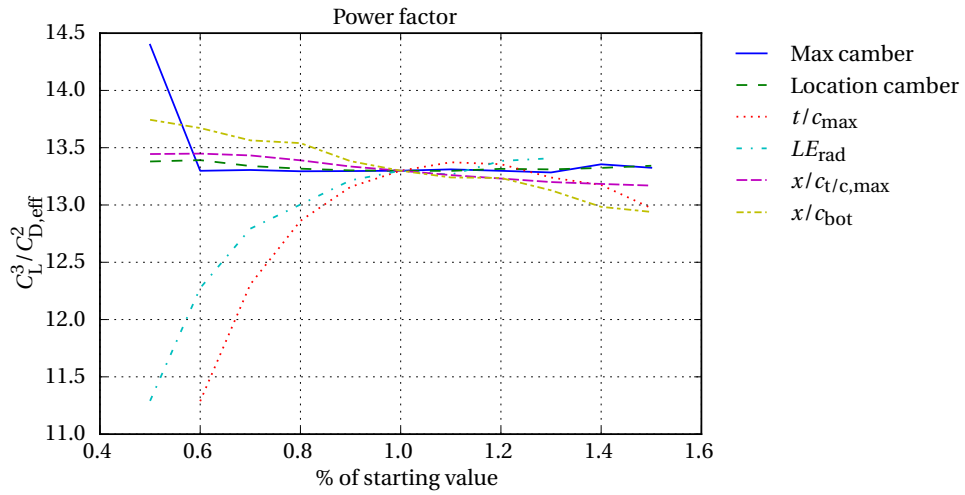

Figure 4.7: $C_L^3/C_{D,eff}^2$ as a function of the design variables

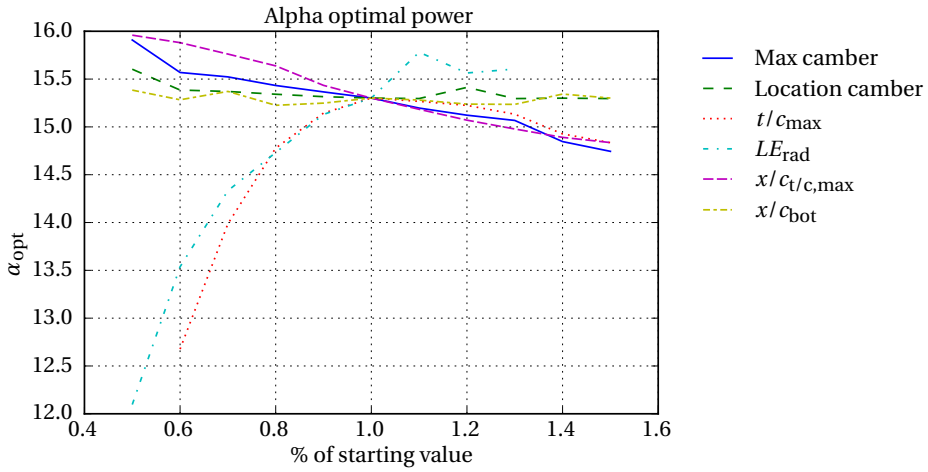

Figure 4.8: α_{opt} as a function of the design variables

interesting if two runs are done, one for $C_{l,max}$ and one for $C_L^3/C_{D,eff}^2$, to see if they converge on different airfoils.

4.3. SUMO optimization

Two optimization runs with SUMO were performed. First, the variable set was reduced to only the thickness and thickness location, with the other 4 variables fixed. Next, the full set was run. Because the 6-dimensional model showed poor prediction capability as shown in section 4.3.2, the results were checked for outliers and a new model was built on the remaining data.

4.3.1. 2D

In this section, the results from the two dimensional model are analyzed. Only t/c_{max} and $x/c_{t/c,max}$ are free variables, while the other 4 are fixed. Their values are given in table 4.1. The same ranges as described in table 3.2 are applied. From the sensitivity study there was only one clear conclusion and that was on x/c_{bot}: this should be as short as possible. Shorter than $x/c = 0.1$ however yields problems with the polynomial definition of the surface. The maximum camber was put at 0 and location of maximum camber was simply just set to a non-zero value. Although the LE_{rad} might still be a parameter of importance in creating a smooth LE, one can see in figure 4.7 that as long as the

LE does not get sharper, it does not have much influence.

In figure 4.9 the result from the toolbox can be seen. The black dots represent the CFD data and the surface represents the model that is built on that data. The surface is then used to obtain a minimum, which only costs a fraction of a second compared to almost an hour per objective function evaluation. In the optimization a manual multi-start is done to ensure finding the global optimum.

Secondly, a validation set is run to assess the predictive capabilities of the model. This can be seen in table 4.2. The predictions hold very well with respect to the CFD-based values. In figure 4.10-4.11 the optimum airfoil and its aerodynamic characteristics are shown. It is relatively thick at 17.4%, with the point of maximum thickness a bit further forward than on a standard NACA 4 series. Compared to what was used as the 'base' airfoil from section 4.2, it performs a little better in both C_l and C_d.

Table 4.1: Values for analysis with reduced number of variables

Parameter	**Value**
c_{max}	0
$x/c_{c,max}$	2
t/c_{max}	free
LE_{rad}	6
$x/c_{t/c,max}$	free
x/c_{bot}	1

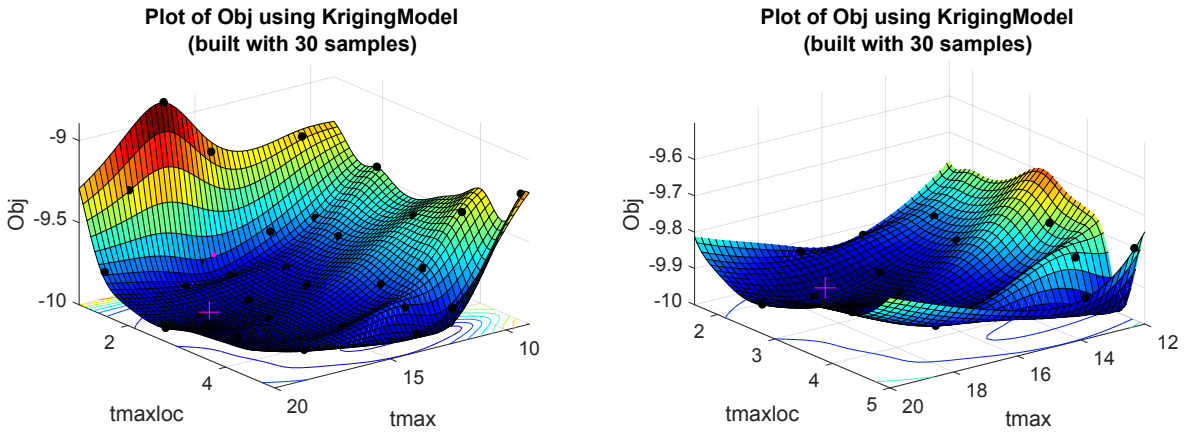

Figure 4.9: 2D model plots with sample data (black dots) and predicted optimum (+). On the left is the full set, on the right a reduced range for the purpose of clarity

Table 4.2: Difference between the validation set and prediction for 2D run

Airfoil coordinate	**CFD**	**Prediction**	**Δ [%]**
0.00-2.00-9.88-6.00-1.94-1.00	-9.60	-9.54	-0.64
0.00-2.00-15.01-6.00-1.39-1.00	-9.82	-9.82	0.02
0.00-2.00-11.30-6.00-3.53-1.00	-9.67	-9.63	-0.39
0.00-2.00-18.74-6.00-1.53-1.00	-9.83	-9.82	-0.09
0.00-2.00-17.42-6.00-2.44-1.00	-9.95	-9.99	0.33

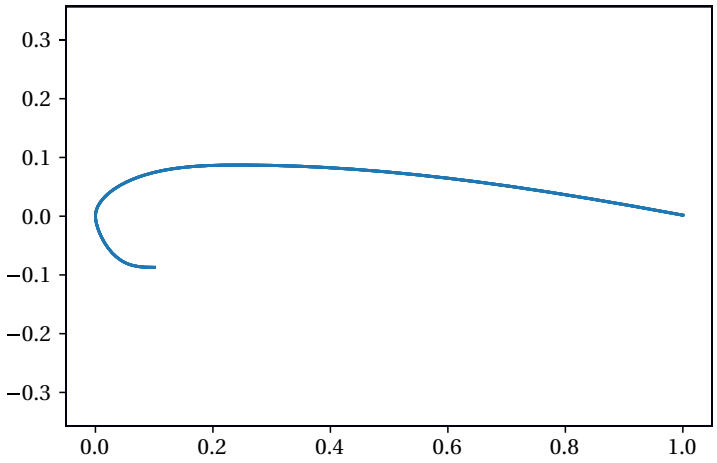

Figure 4.10: Optimum airfoil from the 2D run

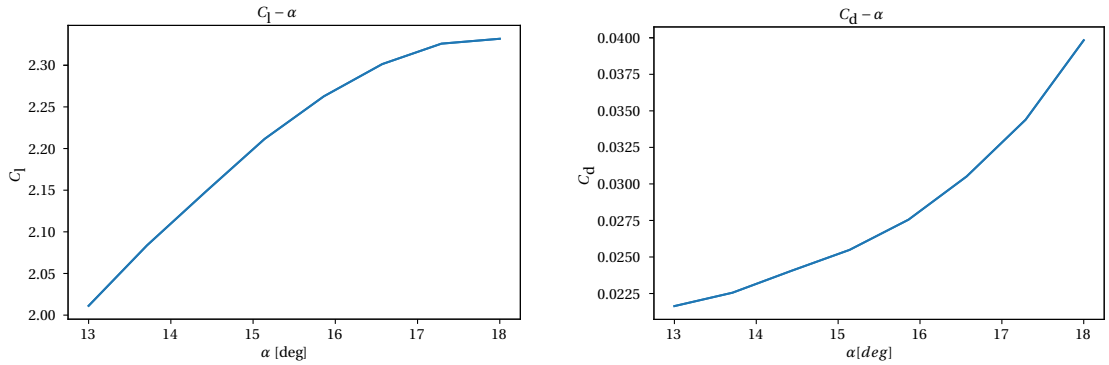

Figure 4.11: Lift curves for optimum airfoil from 2D run

4.3.2. 6D

In the next stage the full set of variables is used. The SUMO toolbox built a model based on 60 samples, or 10 times the number of variables. The results were unsatisfactory. In table 4.3 the difference between the validation set and prediction can be seen. The validation set shows so much deviation that the underlying model can not be trusted. Within the small range of objective function values that is observed ([-10.3 -8.58]), see also figure 4.23), a deviation of 11.76% makes the highest scoring airfoil a mediocre scoring one, at best. The predicted optimum airfoil is shown in figure 4.12.

It is believed that the problem is correlation between design variables. All 6 variables have an influence over the entire airfoil shape and not just locally. This makes it hard to get one global optimum. Also at the edges of the design space, weird interactions can happen. Especially the bottom side of the airfoil is influenced by the camber line definitions. It is concluded that the adapted NACA 4-series parametrization is not suitable for optimization purposes. This could and should have been caught earlier in the process. However, due to the intuitive nature of the variables and the smooth intermediate results from section 4.2, this was not found.

Due to the lack of model accuracy, the second goal to evaluate the samples for $C_{l,max}$ and see if it yields the same result, is not continued. In stead, the results are checked for outliers and a new model is built with the remaining data.

Table 4.3: Difference between the validation set and prediction for 6D run

Airfoil coordinate	**CFD**	**Prediction**	Δ [%]
3.53-4.78-10.05-5.91-3.00-2.89	-9.42	-9.45	0.38
4.63-4.23-16.63-5.06-4.84-1.82	-8.91	-9.62	8.04
3.09-3.59-15.41-5.74-3.14-2.65	-9.36	-9.41	0.58
0.18-2.10-15.17-6.75-3.05-1.76	-9.79	-9.84	0.49
3.37-2.33-19.80-5.59-4.79-1.03	-9.30	-10.38	11.76

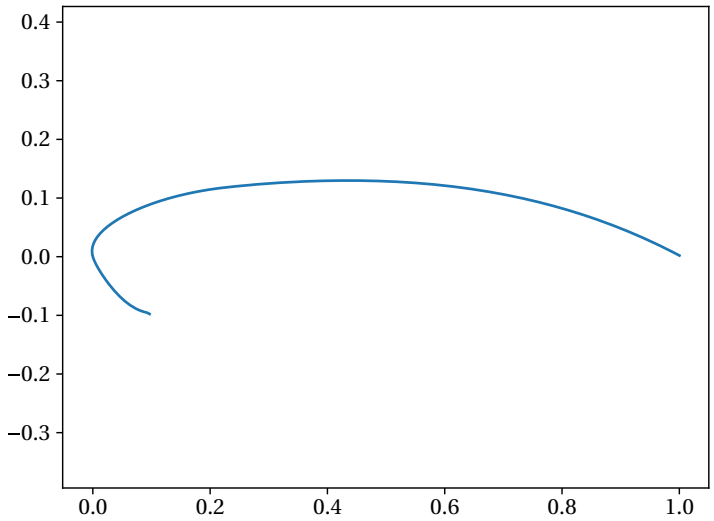

Figure 4.12: Optimum airfoil from the 6D run

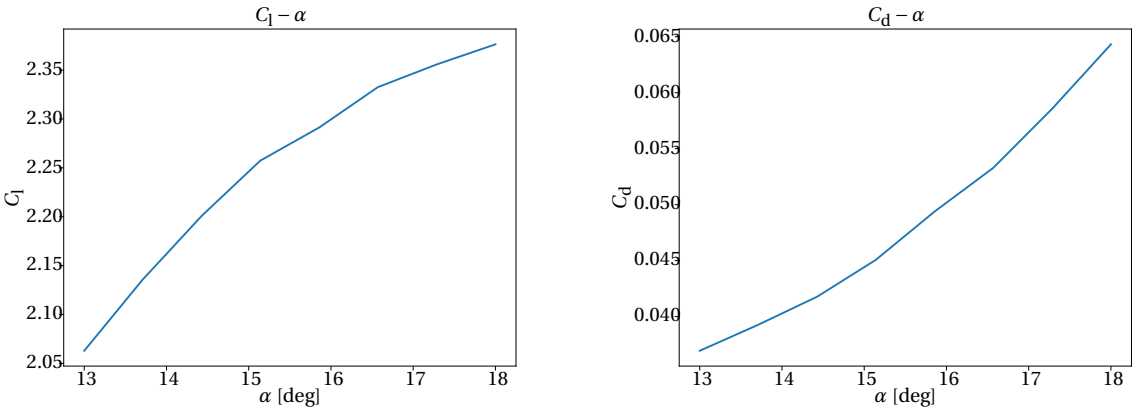

Figure 4.13: Lift curves for optimum airfoil from 6D model

4.3.3. Reduced sample 6D

The toolbox was used to train a model using the same dataset as in section 4.3.2, but with outliers removed. It was judged that actually only the best-performing airfoil from the set was an outlier. Although (almost) converged, the data showed a dip at one α where the drag coefficient was one-third of the neighbouring values. The reason for this is an interaction with the mesh. In most airfoils these α's would diverge and get removed from the results but this managed to obtain a steady state

nonetheless. The same airfoil set as in section 4.3.2 was used, but now with the new optimum added, as can be seen in table 4.4. The predictions are now more accurate. It would be interesting to train the model with extra samples to see if the prediction gets better. On the other hand, as described in section 4.5, it is probably not be worth the effort with the current parametrization.

Table 4.4: Difference between the validation set and prediction for reduced sample 6D run

Airfoil coordinate	**CFD**	**Prediction**	Δ [%]
3.53-4.78-10.05-5.91-3.00-2.89	-9.42	-9.45	-0.03
4.63-4.23-16.63-5.06-4.84-1.82	-8.91	-9.62	6.13
3.09-3.59-15.41-5.74-3.14-2.65	-9.36	-9.41	0.27
0.18-2.10-15.17-6.75-3.05-1.76	-9.79	-9.84	-1.26
3.37-2.33-19.80-5.59-4.79-1.03	-9.30	-9.56	2.87
0.80-2.46-15.00-7.01-2.82-1.02	-9.95	-9.98	0.31

In figures 4.14-4.16 the shape, aerodynamic characteristics and flowfield around the newly found optimum airfoil can be seen. The airfoil has a short x/c_{bot}, medium thickness and, compared to some of the options in the sample set, a smooth nose. In the flowfield it can be observed that the vortex field on the underside is reduced to only one vortex compared to figure 4.1. If this fundamentally benefits performance or is just a coincidence is an interesting topic for future research. Compared to all the airfoils from the previous analyses in terms of C_{l} and C_{d}, the new airfoil performs better over the entire range of α under consideration. For the drag, it only performs better at higher α's. At the lower end, the performance is comparable. The lift is higher over the entire range. Graphs for k and ω can be found in appendix C.

In figure 4.17, the pressure distributions are shown. When comparing them to figure 4.3, there are two main differences. The first is that the wiggle in top-surface C_p at $x/c = 0.2$ is not present. The second difference is that the suction peak at the tip is lower and bit more spread out. This results in both lower drag and higher lift over the entire range of α under consideration.

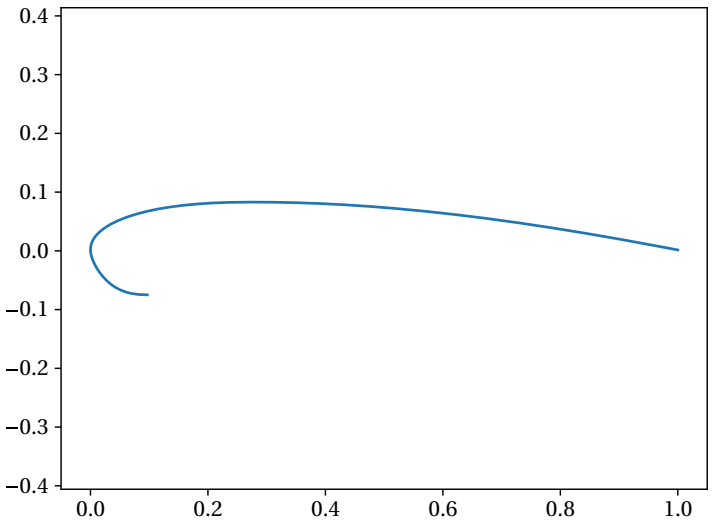

Figure 4.14: Optimum airfoil from the rebuilt 6D model. X = 0.63-2.48-14.98-7.52-3.07-1.00

At this point it is also interesting to compare the resulting airfoil to an actual kite. The center airfoil of one of Kitepower's kites is adapted into a SSK by opening up the LE tube and leaving only

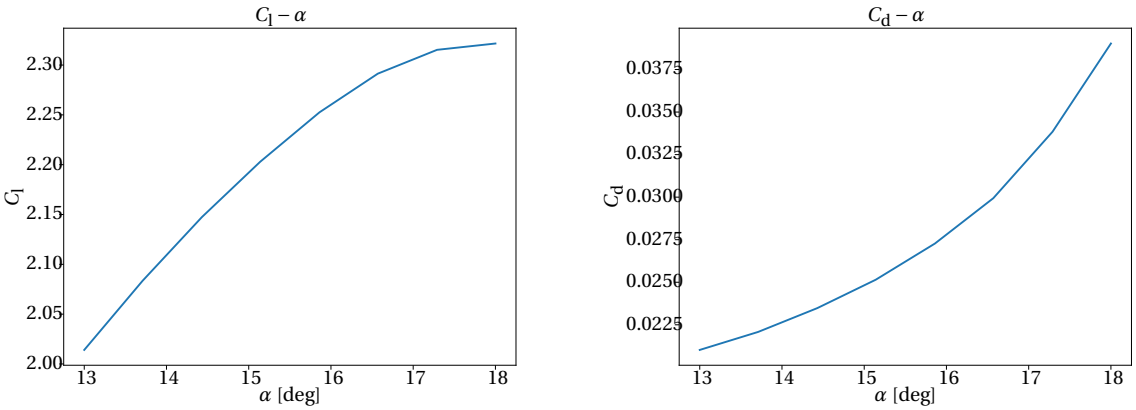

Figure 4.15: Lift curves for optimum airfoil from 2D run

the first quarter. The airfoil is shown in figure 4.18. It should be noted that this is the design profile in the sense that it is non-loaded. The actual shape in flight is unknown. The airfoil has a thickness of 13.29% (from lowest to highest point). Its maximum thickness is quite far forward and has a little recurve going backward. The lift and drag curves are shown in figure 4.19. The maximum $C_L^3/C_{D,\text{eff}}^2 = -9.92$ which is only 0.30% below the result from the optimization.

4.4. Reattachment Point

On the bottom surface of the canopy, the flow reattaches behind the vortex region. To the naked eye it appears that the reattachment point can be approximated by a line from x/c_{bot} in the direction of the undisturbed flow to where it intersects the airfoil. This could be interesting for future simulations because if this point can be predicted, the vortex region may be replaced by a closed airfoil on which simpler flow simulation methods can be used.
One could test this by evaluating the local wall shear stress. In the stagnation point and reattachment point this is 0, because

$$\tau_w = \mu \frac{\partial u}{\partial y} \tag{4.1}$$

and $\partial u/\partial y$ is zero in these points. OpenFOAM has a builtin evaluation function for this called $wallShearStress$. This however only gives one minimum and one maximum. Another option is to estimate it from the C_p distributions in figure 4.3, but these are normalized with the free-stream velocity, and the pressure does not reach the normal stagnation pressure with $C_p = 1$. It is therefore chosen to estimate the location visually.

As can be seen in figure 4.20, it cannot be assumed that it coincides with the location where the undisturbed flow would intersect with the surface. This point is actually in front of that. However,the difference at higher α's is a lot smaller than at low α.

4.5. General considerations

Of all design variables only one gives consistent results: x/c_{bot}. A shorter underside consistently gives better airfoils while a longer one performs worse (see figure 4.22). On the other variables no real conclusion can be drawn. This supports the initial conclusion that the adapted NACA parametrization is not suitable for this purpose. The variables have too much interaction and influence on the whole airfoil. A well performing airfoil therefore is a bit of a game of chance: parameters together should make a smooth airfoil. For instance a really thick airfoil with a small LE_{rad} might still produce a decent airfoil. This also means that the result from a set of variables might not be unique:

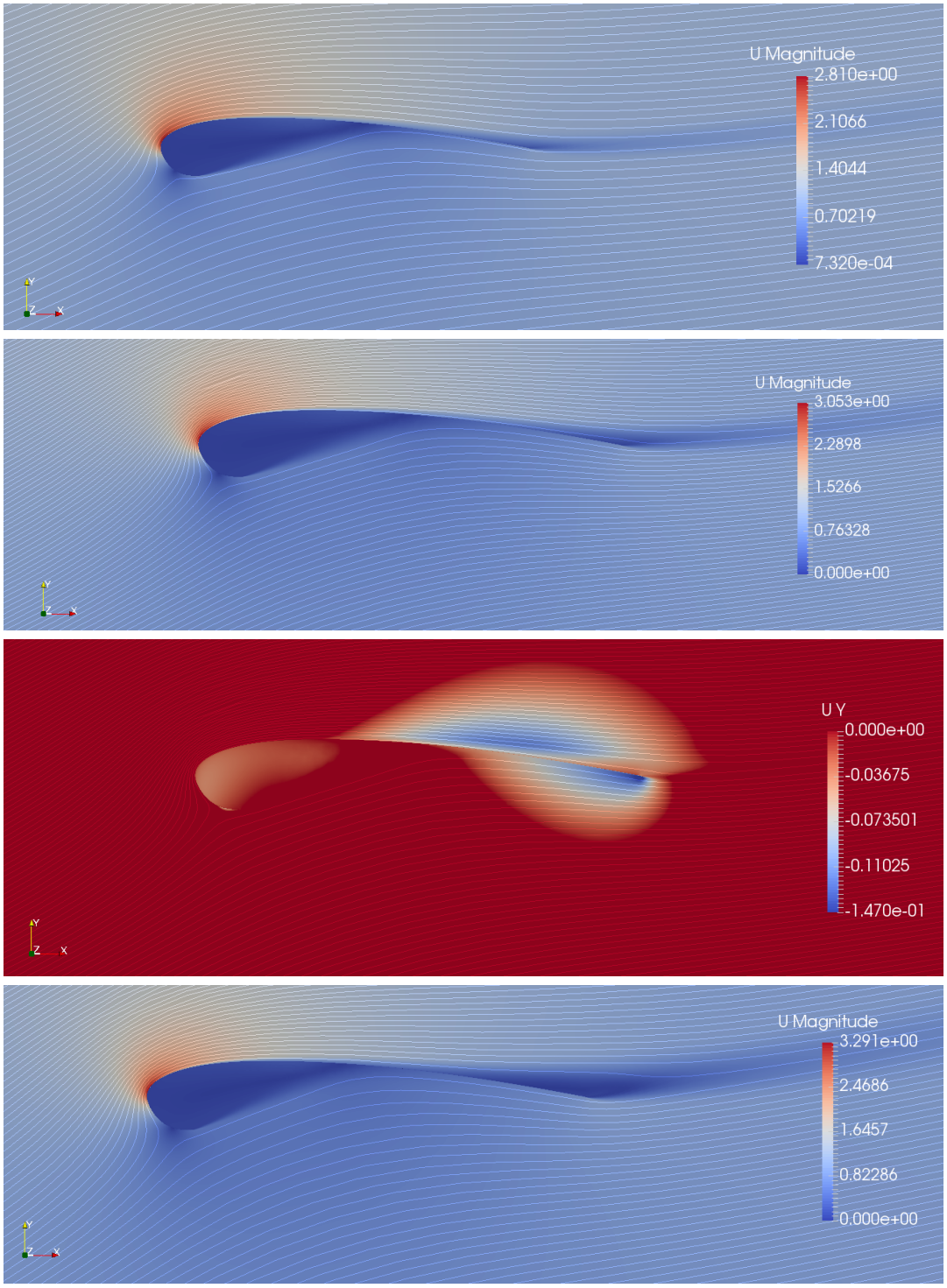

Figure 4.16: Flowfield around optimum airfoil, with from top to bottom: $\alpha = 13°$, $\alpha = \alpha_{opt} = 15.14°$, $\alpha = 15.14°$ with $u_y < 0$ and lastly $\alpha = 18°$

a thick airfoil may be approximated by a thinner one with camber. In figure 4.21 this is shown by plotting 2 airfoils on top of each other. The first is a 0-2-17-6-2-1 and the second is a 1.6-2-14-6-2-1. The top surfaces completely intersect. This example was made to show what can happen. In the simulations, similar airfoils will be closer together, but the extreme was sought out to show its possibilities. In a new parametrization therefore it should be assured that parameters are as orthogonal

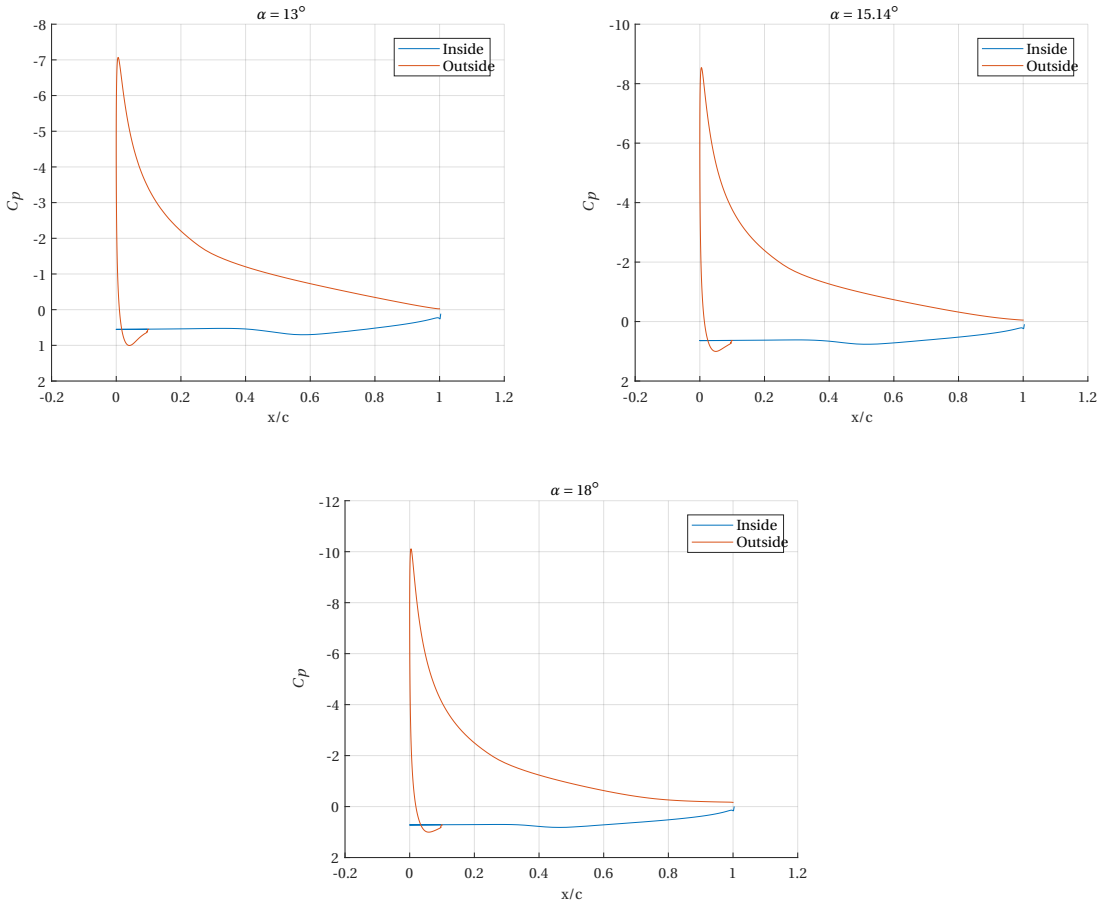

Figure 4.17: Pressure distributions of the optimum airfoil for $\alpha = 13, 15.14$ and $18°$

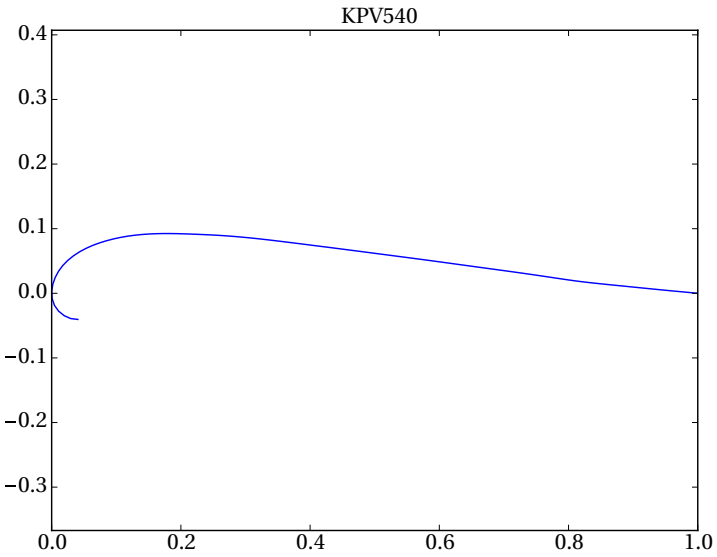

Figure 4.18: Center airfoil for one of Kitepower's kites

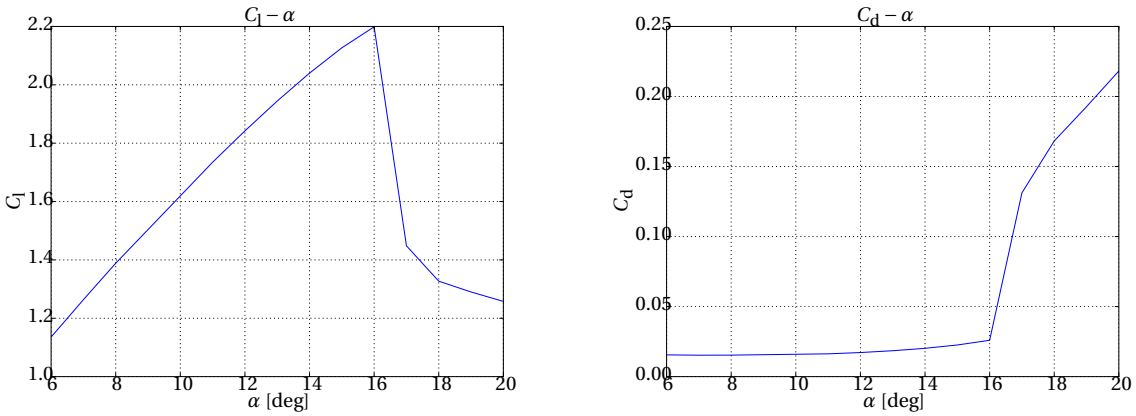

Figure 4.19: Lift curves for the airfoil from figure 4.18

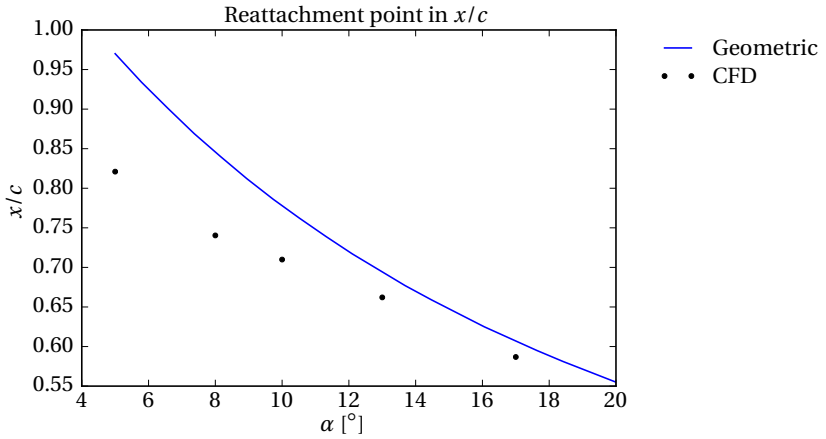

Figure 4.20: Comparison of geometric reattachment point using α and CFD values

as possible, i.e. have as little interaction as possible and provide a unique shape.

Another item to consider is the limited range of objective function values as can be seen in figure 4.23. The optimum airfoil only performs 5.38% better than the mean of $C_L^3/C_{D,\text{eff}}^2 = 9.4137$. A well-designed planform can probably have a much larger influence. This leads to the question to what extent such a high-tech analysis is valuable, other than for general design considerations. It might however be possible that with a better parametrization, the performance can be increased, due to better shape control. As seen in figure 4.9, for large parts of the domain, the result is relatively indifferent to the input values. It can however not be concluded if this is because it a general characteristic of SSK airfoils or due to the parametrization not having enough control over the general airfoil shape.

A general note on the pitching moment coefficient: For all airfoils under consideration this is large compared to a conventional airfoil. Typically $C_m = [-0.3 - 0.2]$ compared to $C_m = [-0.020]$ for a NACA2412 [2]. It is however not taken into consideration because due to the bridle system, the incidence angle is locked. An investigation into the effect of airfoil pitching moment coefficient on a SSK is outside the scope of this project.

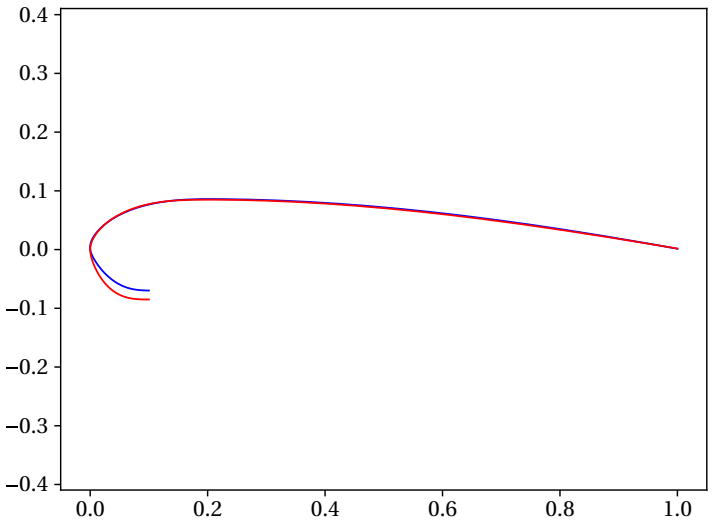

Figure 4.21: Two different airfoils with intersecting top surfaces.

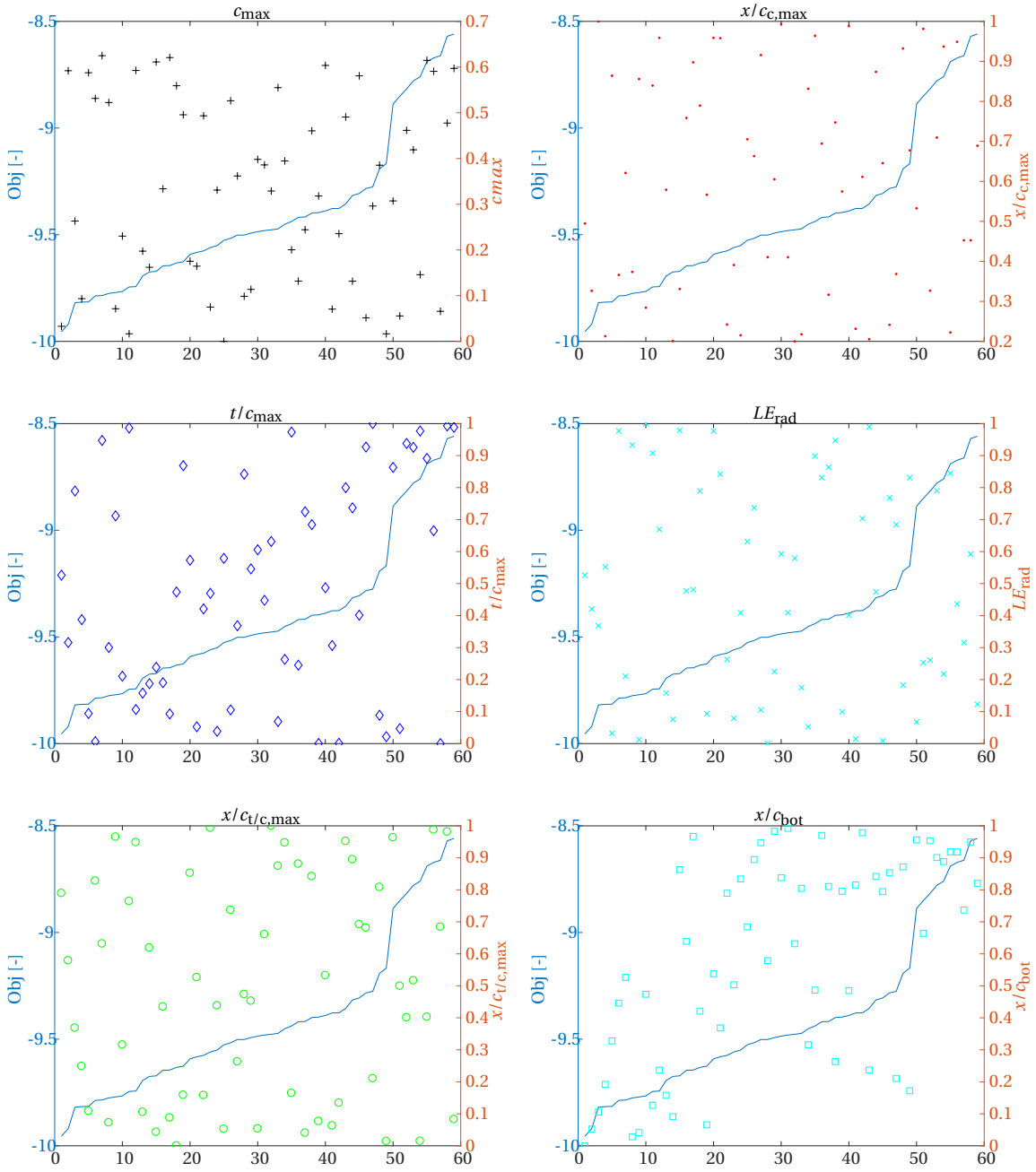

Figure 4.22: Sorted airfoils and their (rescaled) design variables

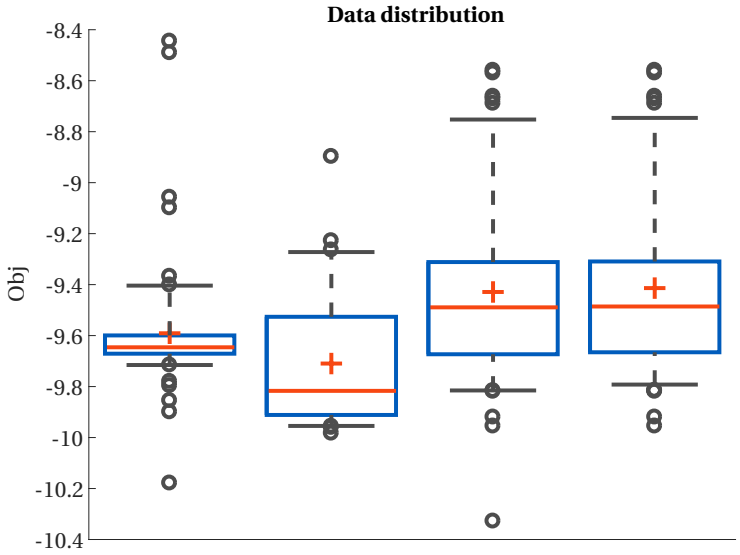

Figure 4.23: Boxplots of the objective function values of the different datasets. From left to right: 1D (sensitivity study), 2D, 6D and 6D with the outlier removed. The red line represents the median, the box holds the second and third quartile and the whiskers extend from 10-90%. The bullets are 'outliers' and the red cross is the mean

5

Conclusion & Recommendations

This chapter holds the conclusions of this project. First the conclusions on the overall process will be described after which recommendations for future research will be made. These recommendations will be split into the two main pillars of this work: The aerodynamics and the optimization.

5.1. Conclusion

In this work, an airfoil for a Single Skin Kite is designed and optimized. Because of the non-orthodox shape of the airfoil, CFD is chosen for airfoil analysis. Due to expected free shear layers and vortices, conventional (viscid-inviscid) airfoil design and analysis codes are not suitable. First a method of automated mesh generation is developed. The method uses a combination of hyperbolic extrusion and unstructured delauney triangulation. For the hyperbolic extrusion, the program *Overture* is used. The unstructured filling of the mesh is done with *gmsh*. The hyperbolic extrusion results in a circular domain, that is orthogonal to all inflow directions. In this way, during optimization, the meshing routine has to be run only once per airfoil and can be used for all angles of attack. For the CFD-analysis, *OpenFOAM* is used with the SIMPLEc algorithm. It is assumed that surface roughness and things like seems will trip the boundary layer into a turbulent state early on. Therefore no transition model was implemented. Built-in post-processing tools are used to gather information about lift and drag characteristics of the airfoil. For numerical optimization, one needs to have a parametrization for the problem at hand. This is a set of variables that describe the design, e.g. an airfoil. In this report, an adapted NACA 4-digit series is chosen and customized to represent a SSK airfoil. An extra variable is added to the five standard ones in the set, to control the length of the bottom skin in the chord-wise direction. The bottom skin also uses this coordinate as the point of maximum thickness. If the bottom skin should in fact be horizontal where it ends, as it is now, should be further investigated. A meshing study is performed to determine a suitable amount of cells in the mesh. The mesh required a relatively large amount of cells around the airfoil. Due to the high degree of turbulence coming from the airfoil, a large computational domain is chosen. Although this added 10% of cells, the computations were greatly sped up since less problems were experienced with balancing boundary conditions. The large domain lets the disturbances of the airfoil die out to free-stream values before they hit the boundary. Next, the outward hyperbolic extrusion mesh was used to compare CFD-results with wind tunnel data for a NACA 2412-63 airfoil. The lack of wind tunnel data concerning kites or similar profiles led to this choice. The lift curves were predicted quite well by the simulations. The drag predictions were not so good. Although the trend was correct, absolute values were off by +37%. Although this is a large deviation, at this point it is assumed that the point of maximum performance is close to stall due to the added drag of the tether that the influence of the airfoil drag is negated. This is also influenced by the lack of alternatives for the

analysis of this type of airfoil. Because the NACA airfoil parametrization uses intuitive parameters like airfoil thickness and camber, a preliminary investigation is made into parameter behaviour for the airfoil. The design variables were individually varied between 0.5 and 1.5 times their reference values of 2-4-12-6-3-2. In this way an intuition for the design space could be developed. It showed that for the $C_l - \alpha$ and $C_d - \alpha$ curves, there are three design parameters that have a relatively low impact on the airfoil performace: maximum camber, location of maximum camber and location of maximum thickness. The other three parameters did show influence, but mainly at the bottom of the range. Low maximum thickness and a sharp LE produced results that can be expected from thin and sharp LE's: they stalled early and have a low $C_{l,max}$. The $C_{l,max}$ showed the same behaviour as $C_L^3/C_{d,eff}^2$, which supported the conclusions from previous work that effectively, optimizing for $C_L^3/C_{d,eff}^2$ means optimizing for $C_{l,max}$. In the next phase the SUMO-toolbox is used for the surrogate modelling process. A Latin hypercube was used as design of experiment. Modelling was done using Kriging and model verification was done using 5-fold cross-validation. As error-metric the root mean square was used. The ratio of initial samples over total samples was one-third. The first run only used t/c_{max} and $x/c_{t/c,max}$ as design variables. The other variables were fixed at $c_{max} = 0$, $x/c_{c,max} = 0.2$, $LE_{rad} = 6$ and $x/c_{bot} = 0.1$. The resulting model was quite invariant. Only at the edges of a thin and a far backward location of maximum thickness, the performance deteriorated significantly. Next, the full set of design variables was used in the optimization. The model was trained with 10 times the number of design variables, as the results from the preliminary analysis were very smooth. The initial results were unsatisfactory. A numerical outlier caused the model to have an optimum where there was no optimum. Also, the results seemed to be independent of design variables. The retrained model from the reduced dataset showed better validation results than the initial model. Like in the 2D model, the results were relatively indifferent to change in variables: the maximum and minimum were within -8.99% and 5.38% of the mean, respectively. The best results seem to come more from a lucky coincidence between variables that provide a "smooth" airfoil than from clear influence of individual variables. Only x/c_{bot} provided this design direction. This parameter however was still limited to $x/c_{bot} = 0.1$, because below that, the parametrization has trouble giving a smooth curve. In general, it can be concluded that the adapted NACA 4-digit parametrization does not work for this application. Finally, the optimized airfoil was compared to a kite currently flown by Kitepower. The adapted airfoil only scored 0.48% below how the optimized airfoil scored. Looking at how different the shapes are, it can be concluded that there might be a lot to still win.

When looking back at the research goals, set out at the start of this report, answers can now be provided. The answer to the first question immediately influences the other ones. Although the chosen parametrization seemed to be very suitable while performing the sensitivity study, it should have been noticed earlier that it is not suitable for optimization purposes. This, together with a low number and the intuitive nature of design variables, made the author oblivious to the lack of real shape control. Another problem is that the variables do not provide a unique shape: the same shape could be approximated by different combinations of parameters. A thicker airfoil can be defined by only the thickness but with zero camber, or a thinner one but with camber. The meshing strategy proved to be reliable for medium to thick airfoils. Thinner airfoils or with a somewhat flat TE angle did not always provide a valid mesh. This problem was undercut in the optimization in two ways: erroneous meshes were recognized and given a *NaN* result and the design space was adapted to only span the space where these problems were not expected. Except the limit on x/c_{bot}, this is not believed to have a significant impact on the overall result. A steady-state RANS solver in the form of the SIMPLEc algorithm was successfully employed for the analysis of the SSK airfoil. Residual convergence to $1 \cdot 10^{-5}$ proved to provide sufficient convergence in the lift and drag characteristics of the airfoil. The sensitivity study was performed by linearly varying the design parameters between 0.5 and 1.5 times a basic value. For this base, a NACA 2412-63-2 was used. A connection between $C_{l,max}$ and $C_l^3/C_{d,eff}^2$ was found, from where it was proposed to run the optimization for both objec-

tive functions. Problems with the parametrization later made the author drop the optimization for $C_{l,max}$. Although surrogate modelling is proposed in literature as the way of optimizing expensive black-box functions, it cannot be concluded if this is the case this time.

5.2. Recommendations

Before one can make more general recommendations, one has to address the parametrization. A different type has to be chosen that produces unique shapes and has more local control. This can for instance be CST-coefficients, which are widely used in airfoil optimization but this option was omitted in this project due to a larger amount of design variables.

Concerning the aerodynamics, there are multiple recommendations. The first one is the lack of validation data for this type of airfoil. A wind tunnel test with a basic airfoil for this class would add a lot of value to the numerical results. Although the meshing and schemes provided very decent results for the NACA 2412, free shear layers, vortex systems and reattachment are common points of problems with CFD analyses. Also, means of identifying faulty data should be refined. The second one is obvious in that this is only a rigid 2D analysis and a kite is a three-dimensional flexible system. This means that both a 3D kite and the FSI problem should be analysed. At a later stage, other methods for aerodynamic analysis like Large Eddy Simulations or Detached Eddy Simulation might be of interest. For the optimization, the objective function itself could be more advanced. Firstly, a range of operation could be used. This would for instance include a range of angles of attack and flight speed ranges, i.e. Reynolds Numbers. To be able to do the range of operation, one would also need a way of improving the estimate of the full kite performance. The assumption of constant airfoil that is discounted with general kite shape parameters is a big assumption and probably needs tuning. Different span-wise stations may require a different objective function. When these are all implemented one might also use one global parameter like minimizing LCOE or maximizing maximum yield for a given rated power. A reliable estimator on yield should then be implemented as well. Concerning the surrogate modelling process, a suitable number of samples should be investigated. Due to the expected smooth behaviour, only ten times the number of design variables was used. With a different number and behaviour of design variables, this should be adapted as well. The other elements of the process: sequential design, model builder (the Kriging) and error measure may need re-evaluation as well, depending on the behaviour of the new variables.

Bibliography

[1] Sumo, 2018. URL http://sumowiki.intec.ugent.be/Running.

[2] Ira H. Abbott and Albert E. Doenhoff. *Theory of wing sections*. Dover Publications, 1959.

[3] Ampyx Power B.V. URL http://www.ampyxpower.com/.

[4] Francois G. Schmitt an. About boussinesq's turbulent viscosity hypothesis: historical remarks and a direct evaluation of its validity. *Comptes Rendus Mecanique*, 335:617–627, 2007. doi: 10.1016/j.crme.2007.08.004.

[5] J. D. Anderson. *Fundamentals of Aerodynamics*. McGraw Hill, 5 edition, 2014.

[6] Andreas Antoniou and Wu-Sheng Lu. *Practical Optimization*. Springer US, 1 edition, 2007. doi: 10.1007/978-0-387-71107-2.

[7] I. Argatov and R. Silvennoinen. Asymptotic modeling of unconstrained control of a tethered power kite moving along a given closed-loop spherical trajectory. *Journal of Engineering Mathematics*, 72(1):187–203, 2012. doi: 10.1007/s10665-011-9475-3.

[8] Ivan Argatov and Risto Silvennoinen. Structural optimization of the pumping kite wind generator. *Structural Multidiscplinary Optimization*, 40(1–6):585–595, 2010. doi: 10.1007/s00158-009-0391-3.

[9] Jeroen Breukels. *An Engineering Methodology for Kite Design*. PhD thesis, Delft University of Technology, 2011. URL http://resolver.tudelft.nl/uuid:cdece38a-1f13-47cc-b277-ed64fdda7cdf.

[10] D. L. Brown, Geoffrey S. Chesshire, William D. Henshaw, and Daniel J. Quinlan. Overture: An object oriented software system for solving partial differential equations in serial and parallel environments. In *Proceedings of the Eighth SIAM Conference on Parallel Processing for Scientific Computing*, 1997.

[11] Antonello Cherubini, Andrea Papini, Rocco Vertechy, and Marco Fontana. Airborne wind energy systems: A review of the technologies. *Renewable and Sustainable Energy Reviews*, 51:1461–1476, 2015. doi: 10.1016/j.rser.2015.07.053.

[12] Antonello Cherubini, Rocco Vertechy, and Marco Fontana. Simplified model of offshore airborne wind energy converters. *Renewable Energy*, 88:465–473, 2016. doi: 10.1016/j.renene.2015.11.063.

[13] K. Crombecq. *Surrogate Modeling of Computer Experiments with Sequential Experimental Design*. PhD thesis, 2011.

[14] Karel Crombecq, Luciano De Tommasi, Dirk Gorissen, and Tom Dhaene. A novel hybrid sequential design strategy for global surrogate modeling of computer experiments. *SIAM Journal on Scientific Computing*, 33:1948–1974, 2011. doi: 10.1137/090761811.

[15] R.M. Cummings, S.A. Morton, W.H. Mason, and D.R. McDaniel. *Applied Computational Aerodynamics*. Cambridge Aerospace Series. Cambridge University Press, 2015. ISBN 9781107053748.

[16] Michael Deaves. An investigation of the non-linear 3d flow effects relevant for leading edge inflatable kites. Master's thesis, 2015.

[17] Mark Drela. *Two-dimensional transonic aerodynamic design and analysis using the Euler equations*. PhD thesis, Massachusetts Institute of Technology, 1985.

[18] Mark Drela. Xfoil: An analysis and design system for low reynolds number airfoils. In Thomas J. Mueller, editor, *Low Reynolds Number Aerodynamics*, volume 54 of *Lecture Notes in Engineering*, pages 1–12. Springer, Berlin-Heidelberg, 1989. doi: 10.1007/978-3-642-84010-4_1.

[19] Storm Dunker. Ram-air wing design considerations for airborne wind energy. In Uwe Ahrens, Moritz Diehl, and Roland Schmehl, editors, *Airborne Wind Energy*, Green Energy and Technology, chapter 31, pages 517–546. Springer, Berlin Heidelberg, 2013. doi: 10.1007/978-3-642-39965-7_31.

[20] C&F Green Energy. Cf100 - 100 kw. Technical report, C&F Green Energy, 2016.

[21] Alexander I.J. Forrester and Andy J. Keane. Recent advances in surrogate-based optimization. *Progress in Aerospace Sciences*, 45:50–79, 2009. doi: 10.1016/j.paerosci.2008.11.001.

[22] Adrian Gambier. Retraction phase analysis of a pumping kite wind generator. In Roland Schmehl, editor, *Airborne Wind Energy*, chapter 6. Springer, 2018.

[23] Sushant S. Garud, Iftekhar A. Karimi, and Markus Kraft. Design of computer experiments: A review. *Computers & Chemical Engineering*, 106:71 – 95, 2017. ISSN 0098-1354. doi: https://doi.org/10.1016/j.compchemeng.2017.05.010. URL `http://www.sciencedirect.com/science/article/pii/S0098135417302090`. ESCAPE-26.

[24] Christophe Geuzaine and Jean-Francois Remacle. Gmsh: A 3-d finite element mesh generator with built-in pre- and post-processing facilities. (79):1309–1331, 2009. doi: 10.1002/nme.2579.

[25] Dirk Gorissen, Ivo Couckuyt, Piet Demeester, Tom Dhaene, and Karel Crombecq. A surrogate modeling and adaptive sampling toolbox for computer based design. (11):2051–2055, 2010.

[26] Christoph Grete. The economic potential of kite power. *Journal of the Society of Aerospace Engineering Students VSV Leonardo da Vinci*, (October):10–11, 2014. URL `http://resolver.tudelft.nl/uuid:f852545f-2946-4556-9ef8-0b5cdbdaf289`.

[27] OpenCFD Ltd (ESI Group). Mesh generation with the blockmesh utility. URL `https://www.openfoam.com/documentation/user-guide/blockMesh.php`.

[28] William D. Henshaw. The overture hyperbolic grid generator user guide, version 1.0. Technical report, Centre for Applied Scientific Computing, Lawrence Livermore National Laboratory, 2012.

[29] Joachim Van Der Herten, Ivo Couckuyt, Dirk DeSchrijver, and Tom Dhaene. Fast calculation of the knowledge gradient for optimization of deterministic engineering simulations. 2016.

[30] W. Hession. Cf50/100 kw turbine, access road, crane, platform, concrete and lifting applications. Technical report, Clean Power Solutions, 2014. URL `http://www.cleanpowersolutions.co.uk/pdf/methodstatement.pdf`.

[31] John Holgate, 2016. URL http://www.extremekites.com.au/uploads/posturls/monthly_2016_01/img-134890-2-fs_peak2_close-up-07.jpg.1040f3b3707801c8027d79a7fec64fe2.jpg.

[32] Ron Kohavi. A study of cross-validation and bootstrap for accuracy estimation and model selection. *International Joint Conference on Arti cial Intelligence*, 1995.

[33] B.E. Launder and D.B. Spalding. The numerical computation of turbulent flows. *Computer Methods in Applied Mechanics and Engineering*, 3:269–289, 1974.

[34] Rachel Leuthold. Multiple-wake vortex lattice method for membrane-wing kites. Master's thesis, 2015.

[35] Miles L. Loyd. Crosswind kite power. *Journal of Energy*, 4(3):106–111, 1980. doi: 10.2514/3.48021.

[36] Makani Power Inc. URL http://www.makanipower.com.

[37] M. D. McKay, R. J. Beckman, and W. J. Conover. A comparison of three methods for selecting values of input variables in the analysis of output from a computer code. *Technometrics*, 21(2):239–245, 1979. doi: 10.2307/1268522.

[38] M.R. Mendenhall and S.B. Spangler J.N. Nielsen. Investigation of methods for predicting the aerodynamic characteristics of two-lobed parawings. Technical Report CR-1166, Nielsen Engineering & Research, inc, for NASA Langley Research Center, 1968.

[39] FR Menter. Improved two-equation k-omega turbulence models for aerodynamic flows. Technical Report 103975, NASA, 1992.

[40] W. J. Ockels. Wind-driven driving apparatus employing kites, 6 2000.

[41] Wubbo Johannes Ockels. Laddermill, a novel concept to exploit the energy in the airspace. *Journal of Aircraft Design*, 4(2-3):81–97, 2001. doi: 10.1016/s1369-8869(01)00002-7.

[42] Johannes Oehler and Roland Schmehl. Aerodynamic characterization of a soft kite by in situ flow measurement. *Wind Energy Science, in review*, pages 1–25, 07 2018. doi: 10.5194/wes-2018-46.

[43] Reinhart Paelinck. The quest for cheap cl max. 2016.

[44] Xaver Paulig, Merlin Bungart, and Bernd Specht. Conceptual design of textile kites considering overall system performance. In Uwe Ahrens, Moritz Diehl, and Roland Schmehl, editors, *Airborne Wind Energy*, Green Energy and Technology, chapter 32, pages 547–562. Springer, Berlin Heidelberg, 2013. doi: 10.1007/978-3-642-39965-7_32.

[45] Peter R. Payne and Charles McCutchen. Self-erecting windmill, october 1976.

[46] L. Prandtl. Uber die ausgebildeten turbulenz. (5):136–139, 1925.

[47] Benoit Python. Methodology improvement for performance assessment of pumping kite power wing. Master's thesis, 2017.

[48] Christopher Rumsey. 2dn00: 2d naca 0012 airfoil validation case, 2014. URL https://turbmodels.larc.nasa.gov/naca0012_val.html.

[49] Roland Schmehl, editor. *Airborne Wind Energy*. Springer Singapore, 2018. doi: 10.1007/978-981-10-1947-0.

[50] Roland Schmehl, Michael Noom, and Rolf van der Vlugt. Traction power generation with tethered wings. In Uwe Ahrens, Moritz Diehl, and Roland Schmehl, editors, *Airborne Wind Energy*, Green Energy and Technology, chapter 2, pages 23–45. Springer, Berlin Heidelberg, 2013. doi: 10.1007/978-3-642-39965-7_2.

[51] SkySails GmbH. URL `http://www.skysails.com`.

[52] P. Spalart and S. Allmaras. A one-equation turbulence model for aerodynamic flow. In *Proceedings of the 30th Aerospace Sciences Meeting and Exhibit*, Reno, NV, USA, 1992. doi: 10.2514/6.1992-439.

[53] Andrea Sylvestri. Airborne wind energy: Fluid structure interaction analysis of a wing section of a single skin "peak 2" kite. Master's thesis, 2015.

[54] Karel Van Velden. Surrogate modelling for airfoil shape optimization. Master's thesis, 2017.

[55] Andrea Venturato. Analisi fluidodinamica del profilo alara clark-y ed ottimizzazione multi-obbiettivo algoritmo genetico. Master's thesis, 2013.

[56] H.K. Versteeg and W. Malalsekera. *Introduction to Computational Fluid Dynamics*. Pearson Education Limited, 2nd edition, 2005.

[57] Felipe A.C. Viana, Gerhard Venter, and Vladimir Balabanov. An algorithm for fast optimal latin hypercube design of experiments. *International Journal for Numerical Methods in Engineering*, 82:135–156, 2010. doi: 10.1002/nme.2750.

[58] H. G. Weller, G. Tabor, H. Jasak, and C. Fureby. A tensorial approach to computational continuum mechanics using object-oriented techniques. *Computers in Physics*, 12(6), 1998. doi: 10.1063/1.168744.

[59] D.C. Wilcox. *Turbulence Modeling for CFD*. DCW Industries, Inc., 1st edition, 1993.

A

Airfoil coordinates

Table A.1: Airfoil coordinates for 2412-63-2 SSK airfoil

X	**Y**	**X**	**Y**
0.200000	-0.059925	0.266769	0.077641
0.185093	-0.059853	0.296073	0.078669
0.167365	-0.059550	0.326230	0.079213
0.144624	-0.058627	0.357108	0.079257
0.123274	-0.056946	0.388574	0.078776
0.103384	-0.054415	0.420330	0.077786
0.085025	-0.051019	0.452315	0.076386
0.068269	-0.046808	0.484487	0.074591
0.053185	-0.041883	0.516711	0.072415
0.039848	-0.036383	0.548852	0.069878
0.028325	-0.030467	0.580775	0.067004
0.018684	-0.024304	0.612347	0.063826
0.010984	-0.018052	0.643438	0.060379
0.005278	-0.011851	0.673920	0.056702
0.001607	-0.005810	0.703666	0.052838
0.000000	-0.000000	0.732555	0.048833
0.000466	0.005725	0.760469	0.044732
0.003005	0.011527	0.787296	0.040585
0.007611	0.017383	0.812928	0.036438
0.014275	0.023260	0.837261	0.032340
0.022977	0.029114	0.860198	0.028336
0.033688	0.034896	0.881648	0.024473
0.046370	0.040547	0.901526	0.020792
0.060976	0.046007	0.919753	0.017334
0.077452	0.051213	0.936259	0.014135
0.095729	0.056103	0.950978	0.011231
0.115735	0.060620	0.963852	0.008651
0.137384	0.064711	0.974832	0.006421
0.160585	0.068332	0.983874	0.004566
0.178926	0.071052	0.990943	0.003103
0.197114	0.072719	0.996013	0.002048
0.217675	0.074299	0.999062	0.001411
0.238445	0.076107	1.000080	0.001197

B

Flow characteristics 2412-63-2

The ω-plots in figure B.2 have been rescaled to a maximum of $\omega = 800$. The maximum values in the datarange is $\omega \approx 1 \cdot 10^7$. The red spots in the boundary layer are in fact smooth, but this is not visible in the overview plots.

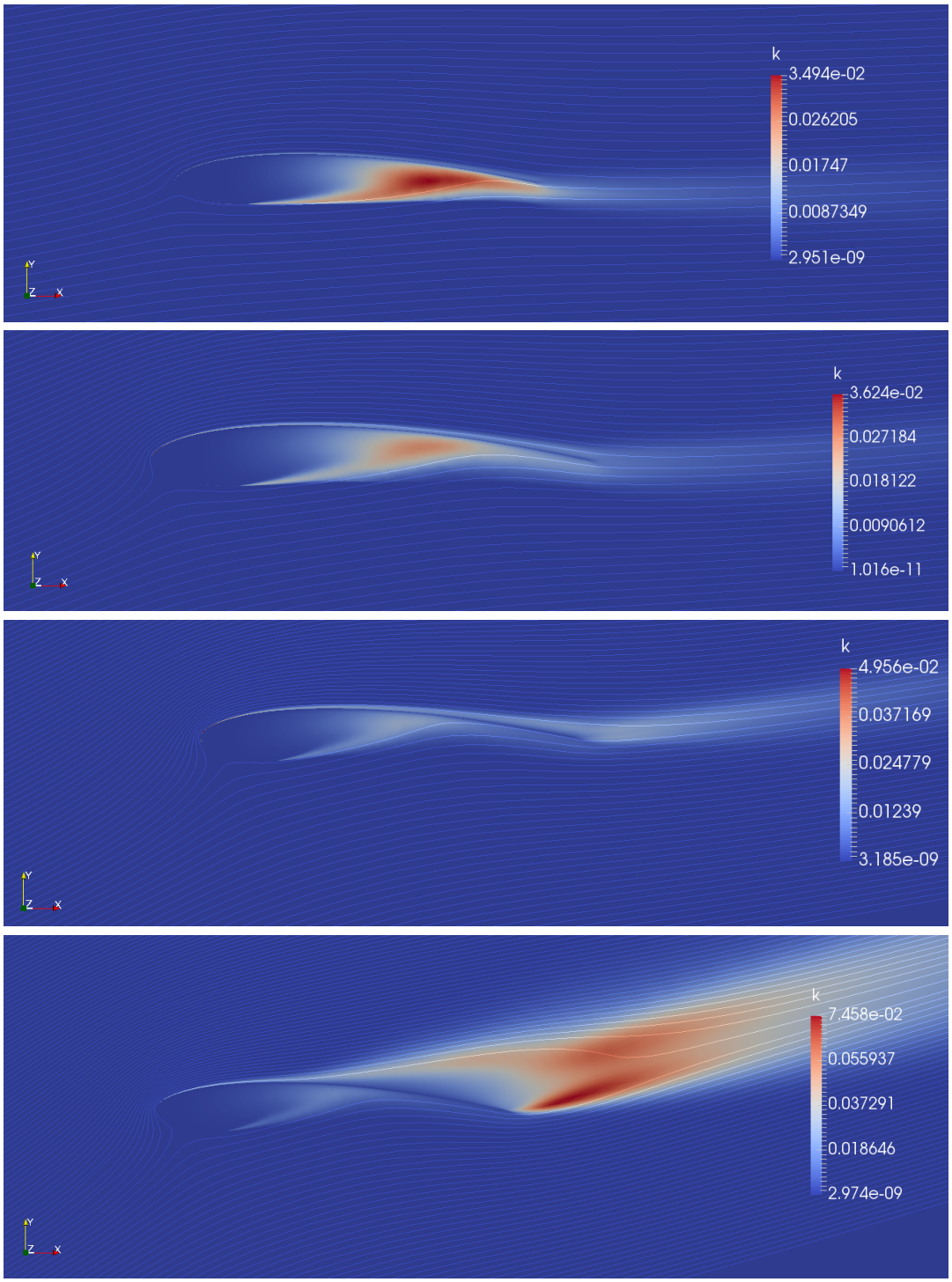

Figure B.1: Flowfield around 2412-63-2 for turbulent kinetic energy, k

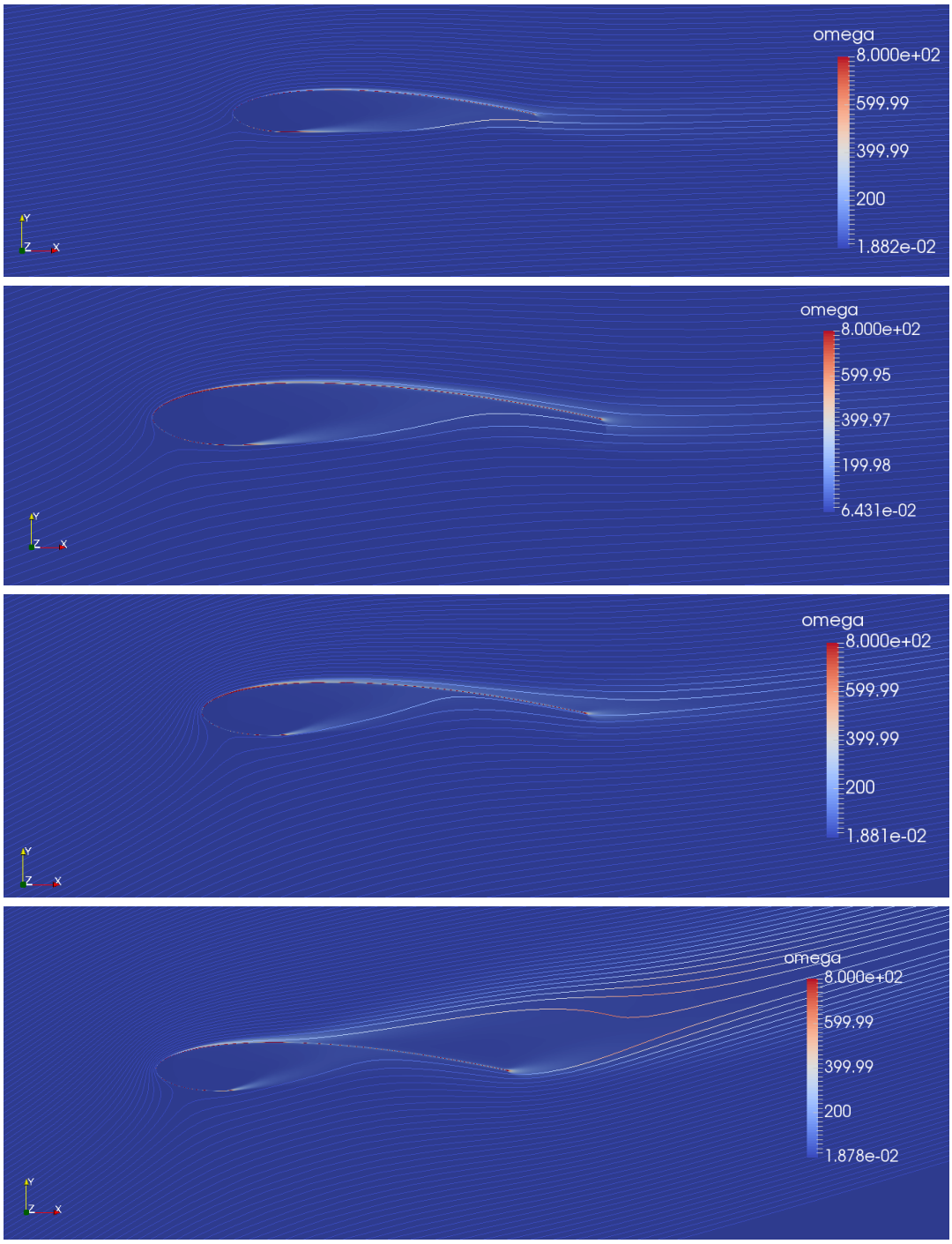

Figure B.2: Flowfield around 2412-63-2 for specific dissipation rate, ω

C

Flow characteristics 0.80-2.46-15.00-7.01-2.82-1.02

The ω-plots in figure C.2 have been rescaled to a maximum of $\omega = 800$. The maximum values in the datarange is $\omega \approx 1 \cdot 10^7$. The red spots in the boundary layer are in fact smooth, but this is not visible in the overview plots.

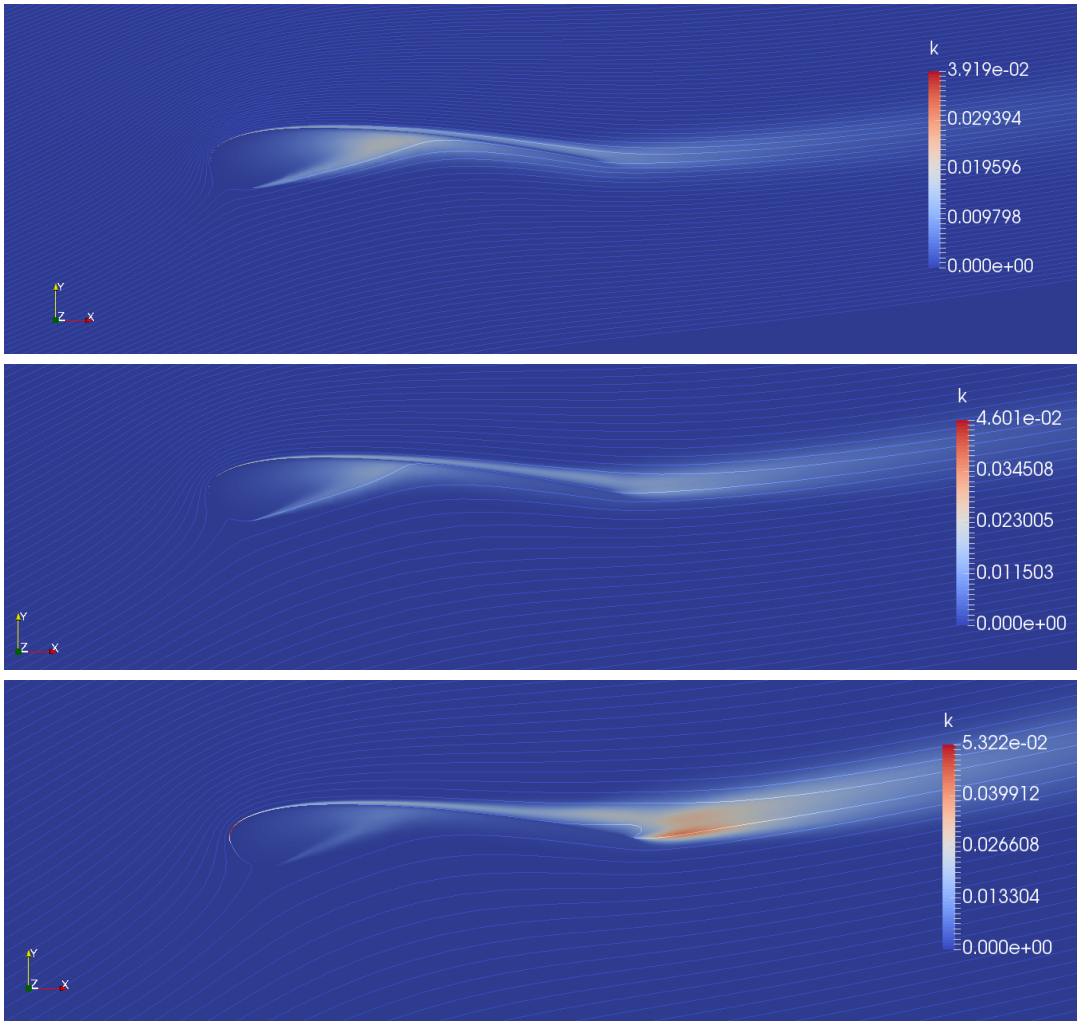

Figure C.1: Flowfield around 0.80-2.46-15.00-7.01-2.82-1.02 airfoil for turbulent kinetic energy, k

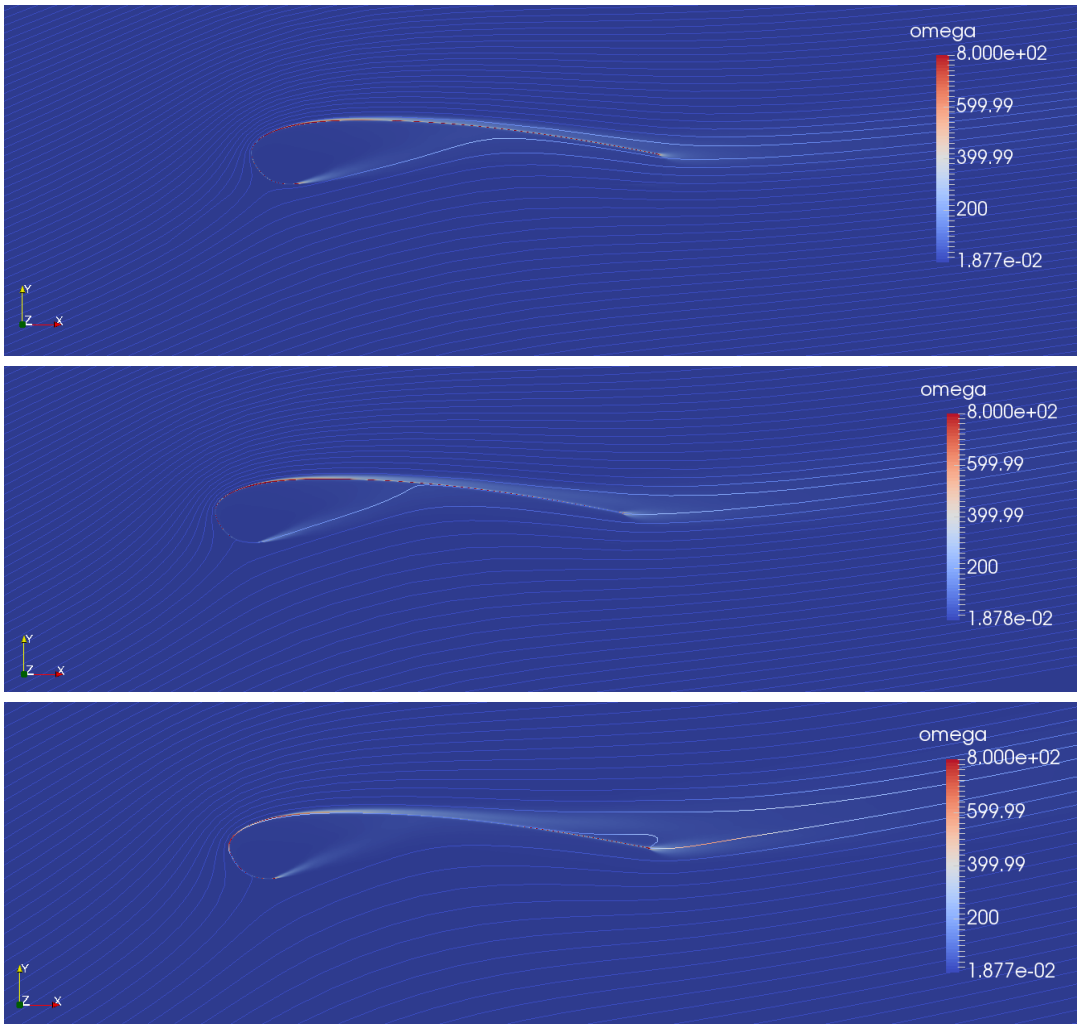

Figure C.2: Flowfield around 0.80-2.46-15.00-7.01-2.82-1.02 for specific dissipation rate, ω